Study of volumetric origami structure with highly anisotropic and tunable load carrying capacity

Balakumaran Gopalarethinam

A thesis
submitted in partial fulfillment of the
requirements for the degree of

Master of Science

University of Washington

2018

Committee:

Jinkyu Yang

Per Reinhall

Sawyer Fuller

Program Authorized to Offer Degree:
Mechanical Engineering

University of Washington

Abstract

Study of volumetric origami structure with highly anisotropic and tunable load carrying capacity

Balakumaran Gopalarethinam

Chair of the Supervisory Committee:
Professor Jinkyu Yang
Department of Aeronautics and Astronautics

Deployable structures have been of great interest for applications like space structures and portable architectures. However, these deployable structures often suffer from the lack of capabilities to support external load on their own. Thus, there is a high demand for a deployable yet rigid, load supporting structure. Here, I investigate analytically and experimentally the ability of an origami-based structure called the Tachi Miura Polyhedron (TMP), which can be used as deployable yet rigid structure. The TMP is a three dimensional origami structure representing bellows in appearance. It exhibits some unique mechanical properties, and here in particular, its force-displacement response is studied to establish its novel response mathematically. First, the force-displacement relations for the single TMP cell are developed in three mutually perpendicular directions of compression and are verified by experiments on paper prototypes. It is found that the single TMP exhibits a highly tunable load carrying ability under compression in one direction and tunable anisotropic behavior, i.e. variable load capacity depending on the loading directions and initial postures. This makes it a suitable choice for deployable yet rigid structures. Then the force displacement relations are extended to a multi-TMP structure in which multiple TMP cells are combined to form a cellular structure. It is found that the multi-TMP also exhibits tunable load capacity and tunable anisotropic behavior. Conclusively highly tunable and anisotropic load

carrying mechanisms of the TMP are understood and established mathematically through this work, and the ability of this structure to be deployable yet load supporting is showcased by simple prototypes.

TABLE OF CONTENTS

LIST OF FIGURES

ACKNOWLEDGMENTS

I would like to sincerely thank Professor Jinkyu Yang for giving me the opportunity to work on this research work at the Laboratory for Engineered Materials and Structures and for guiding me all through this research. I am highly grateful to Dr. Hiromi Yasuda, who has mentored me and guided me with his time and efforts in all phases and aspects of this research work. I would also like to thank Professor Kunimine from University of Kanazawa in Japan who has been of great help during the experimental phase of this research work. And many thanks to Professor Per Reinhall and Professor Sawyer Fuller for accepting to be the committee members for this thesis and providing their guidance towards completion of this work. Last but not least, I would like to thank the UW Comotion for their help with prototyping resources.

DEDICATION

To my ever-supportive Family.

Chapter 1

INTRODUCTION

Background and Motivation

In recent days, there has been great deal of interest towards deployable structures which can be portable and compact when not in use [1] [2]. The reason for this interest is obviously space constraint. There are aerospace applications for which weight and space savings are always top priority. It is important that devices to be carried into outer space are made of deployable structures so that they can fit in a compact manner in the space shuttles and then deployed once in outer space. Then there are application areas like cardiovascular surgeries where there is a need for deployable stents. There are traditional mechanisms like scissors lift and telescopic cylinders which serve the need for compact storage in traditional cases of architecture and aerospace [3] [4]. But there is one problem with these mechanisms. These mechanisms cannot support load on their own. Then there are also inflatable structures which will be stored in their deflated state and deployed by inflation [5]. They can support loads on their own but those materials are not stiff or rigid enough for harsh environments.

Thus there is a lack of deployable structures which can support load and be rigid. This quest for deployable structures which are capable of maintaining the deployed state on their own and support load in the deployed state is the motivation for this research work. One class of deployable structures which have been greatly studied in recent time and which can be the answer for the quest of this research is the structures based on the ancient Japenese art of paper folding, origami. Origami based structures are obtained by combining the different types of folds in origami in a certain fashion. Such structures have been used in some of the wide range of engineering applications discussed above, e.g.,Deployable stents for the cardiovascular surgeries [6] and deployable solar sails to capture solar power in the outer

space [7] [8]. There are also some origami cellular metamaterials shown to possess certain degree of deployability and load carrying capacity at its deployed state [9]. So I decided to research the origami based structures for the purpose of this work.

One of the famous origami folds is the miura ori. One kind of structures developed using miura ori are the two dimensional shell type structures [10]. The other kind is the foldable volumetric structures [11]. One such three dimensional volumetric structure is called the Tachi-Miura Polyhedron (TMP) [12]. The TMP can contain a volume and it has novel kinematic characteristics [13]. The geometry of TMP has been characterized and it is understood that the TMP can show tunable static mechanical properties such as negative poisson's ratio and negative stiffness. The structure exhibits foldability under axial loading and thus it was seen as a good choice for deployable structures [13] [14]. The TMP structure seems to possess lot of unique characteristics and there is potential for this structure to be the answer for the quest of this research which is to be deployable and self-supporting and load carrying at its deployed state.

Objective

The goal of this research was to develop force-displacement relations for the TMP under compression loading and verify them experimentally. This should help undertanding whether this is a fit for the quest of the research and also help towards designing the structure for real-time applications. In addition, other interesting properties of the structure were explored and this will pave the way for other application areas as well.

Methodology

In this work, the static force-displacement relations for single TMP were developed first and then they were verified experimentally. These relations are then extended to multi-cellular structure composed of many single TMP cells. The unique behaviors of the structure under compression loading are understood and the structure is shown to be a good choice for deployable yet load supporting and stiff structure.

This thesis document is structured in the following manner. The geometry of the TMP unit cell is explained in detail in chapter 2. This forms the basis for derivation of the force-displacement relations of the TMP under 3 mutually perpendicular directions of compression which are explained in detail in the chapter 3. The tunable load carrying capacity and anisotropicity of the single TMP is explained in this chapter. The experimental verification is explained in detail in chapter 4. Then, the multi-cellular structure which can be developed by combining the TMP unit cells is introduced in chapter 5. The force-displacement relations and the tunable anisotropicity of the multi-TMP structure are compared with that of the single-TMP in this chapter. Finally some prospective applications for this novel structure and future work which can be done on this structure are listed in Chapter 6.

Chapter 2

GEOMETRY OF TMP

The TMP is a 3-dimensional structure which represents bellows in appearance and motion. The TMP is built by placing numerous layers consisting of opposing miura-ori folds, which is one of the primary origami folds, one over the other and then joining one stack of layers with another stack of layers. The two stacks are mirrored forms of each other. The single TMP cell and its folding motion is shown in figure 2.1. Though it seems to be a very irregular geometry at first sight, it can be defined using some length and angle parameters so that the geometry can be made in a repeatable fashion. These geometric parameters are introduced in this chapter.

The geometry of TMP has been previously characterized [13] by three length parameters

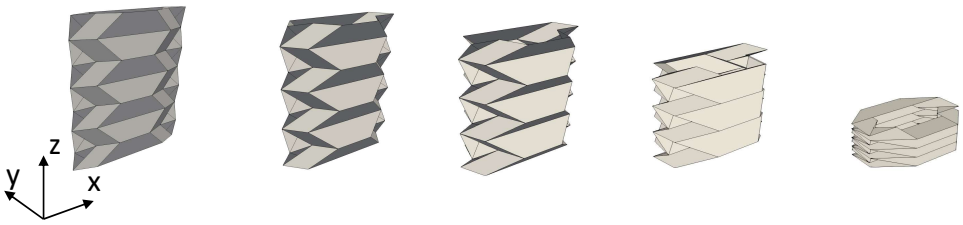

Figure 2.1: Folding Motion of TMP (See left to right)

l, m, d, an inner parellelogram angle α and three folding angles θ_M, θ_S, and θ_G. They can be understood by using two layers of the TMP. The two layers of the TMP are shown in part A of the figure 2.2. The other parts of figure 2.2 define the folding angles θ_M, θ_G and θ_S. Now, θ_M is called as the main folding angle while θ_S, and θ_G are called as side folding angles. The width, breadth, and height of the structure are called W, B and H respectively. They are also defined in figure 2.2 .

Please note that $\theta_M \in [0, 90°]$, $\theta_S \in [0, 90°]$, and $\theta_G \in [0, 2\alpha]$. $\theta_M = 90°$ defines the flat state of the TMP. This is shown in part A of figure 2.3. The length parameters are defined in the flat state of the TMP and they are defined in the part B of the figure 2.3. Part B of figure 2.3 shows the crease pattern of the front of the two sheets that make up the TMP and part C of figure 2.3 shows the crease pattern of the back sheet. The horizontal solid lines represent the main crease lines and the inclined dotted lines represent the sub crease lines.

The folding angles change in value during the folding motion of the TMP while the length parameters and α do not. θ_S, and θ_G are derived quantities of θ_M. The geometrical relations between the three angles are as follows [13]:

$$\tan\frac{\theta_G}{2} = \tan\alpha\cos\theta_M \tag{2.1}$$

$$\sin\frac{\theta_G}{2} = \sin\alpha\cos\theta_S. \tag{2.2}$$

The width, breadth and height of the structure are calculated using the length parameters and α. The formulae to calculate B, W and H are as follows [13]:

$$\begin{aligned} B &= 2m\sin\theta_G + d\cos\theta_M \\ W &= 2l + \frac{d}{\tan\alpha} + 2m\cos\theta_G \\ H &= Nd\sin\theta_M. \end{aligned} \tag{2.3}$$

The TMP has been shown to exhibit negative poisson's ratio [13] and this is because of unique variation of B and W with respect to θ_M. As the structure folds, the main folding angle θ_M decreases and with it, height H of structure also decreases. For engineering materials in general, with decreasing height, breadth and width would increase but TMP shows decreasing width for all configurations and decreasing breadth for certain configurations. This can be understood by considering TMP of two α values - 45° and 70°. The variation of B and W with θ_M is shown for TMP of configuration: $l = 40$ mm; $m = 30$ mm; $d = 30$ mm; $\alpha = 70°$ and 45°; $N = 7$ in figure 2.4.

TMP of both α configurations show decreasing width with decreasing θ_M.TMP of α - 45° shows increasing breadth for decreasing θ_M. This is normal behavior. But TMP of α -

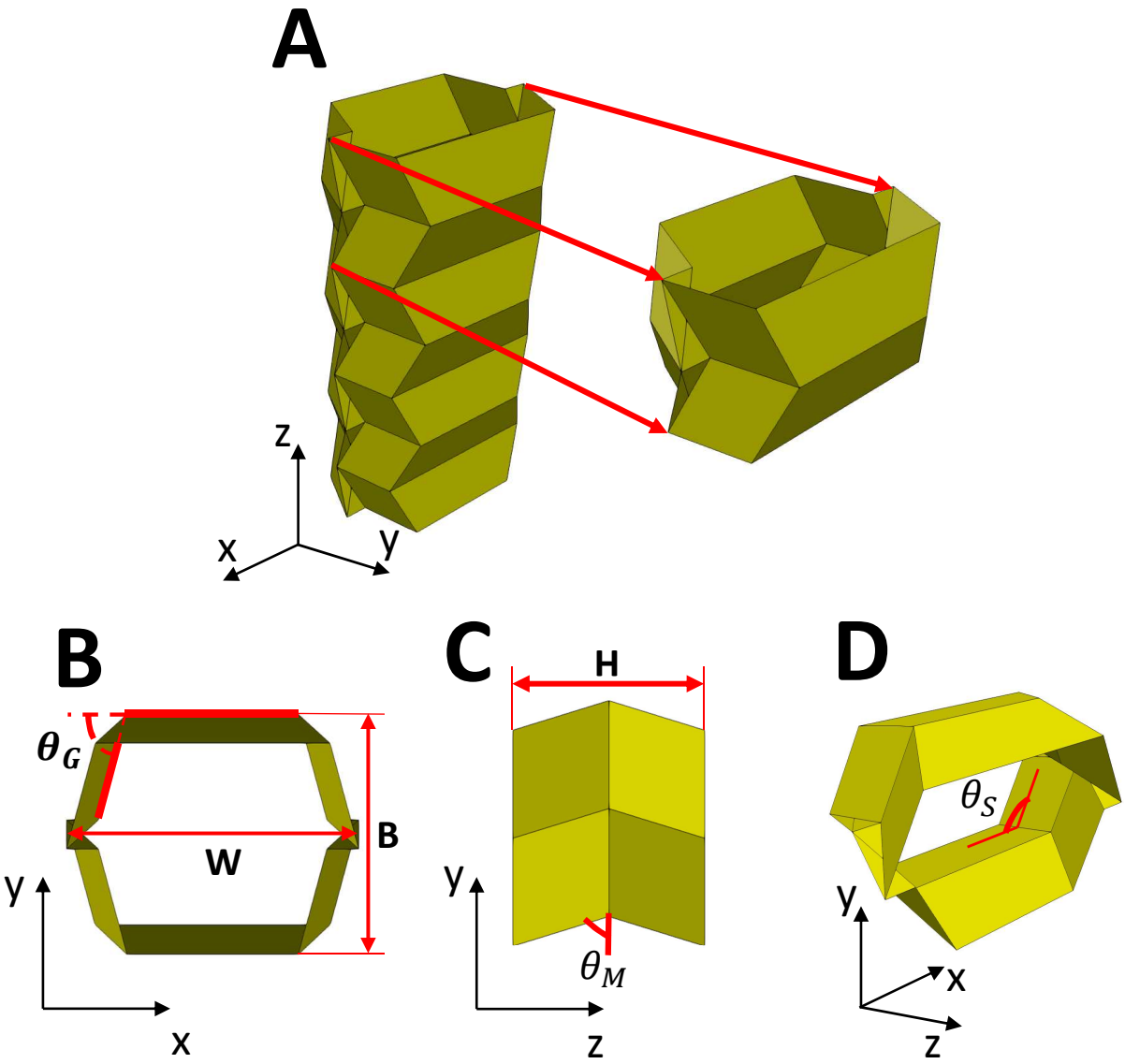

Figure 2.2: Folding Angles of TMP- A)Two layers of TMP to define folding angles; B) Top view showing folding angle θ_G, Breadth B, and Width W of the structure; c) Side view showing Folding angle θ_M and height H of structure; D) Isometric view showing folding angle θ_S.

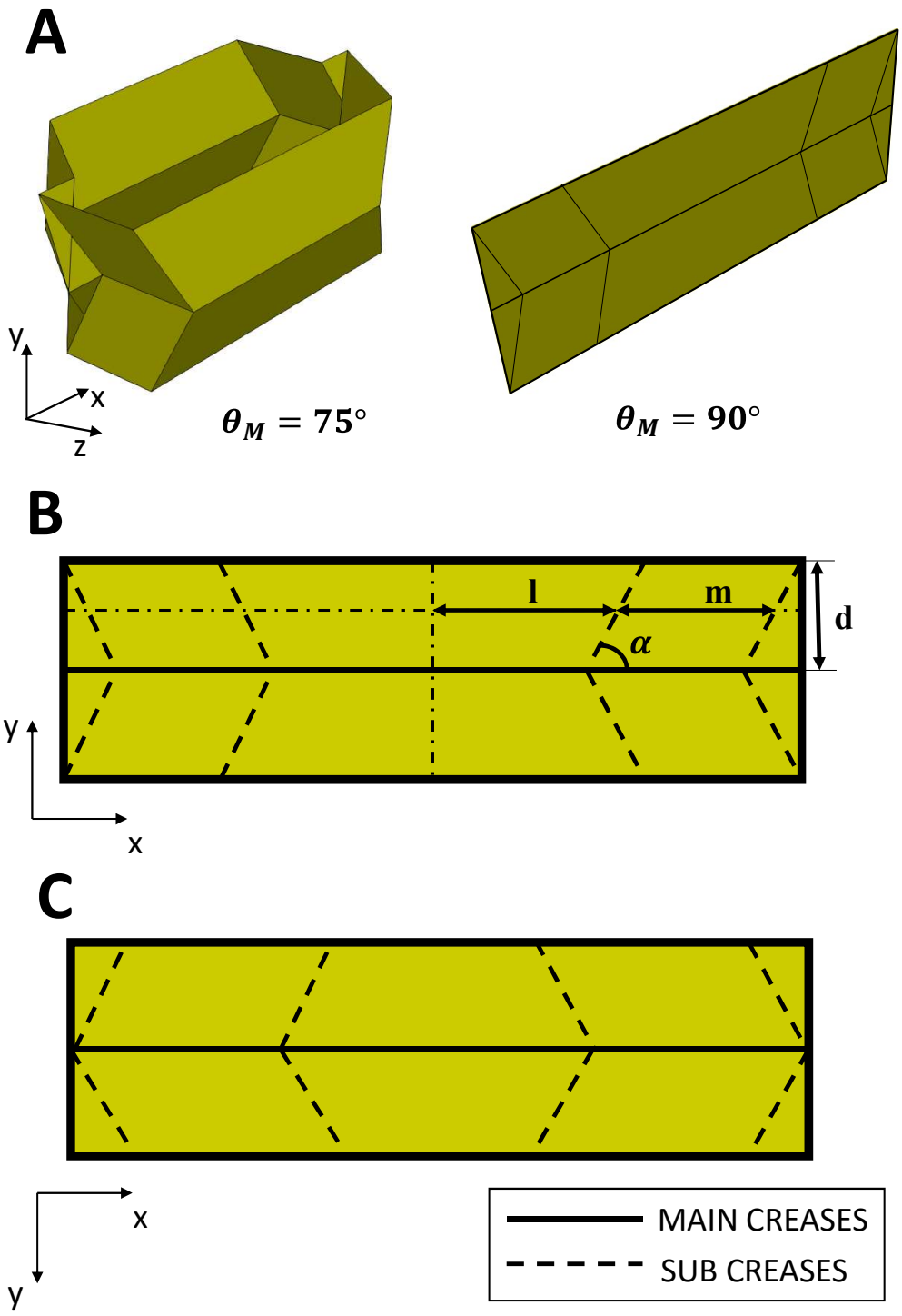

Figure 2.3: Geometric Parameters of TMP- A) Two layers of the TMP - left image is $\theta_M = 75°$ and right image is $\theta_M = 90°$; B)Front view of two layers of TMP in the flat state with $\theta_M = 90°$ showing the length parameters and α angle. It also shows the crease pattern of the front paper; C) Back view of TMP in flat state showing the crease pattern of back-side paper;

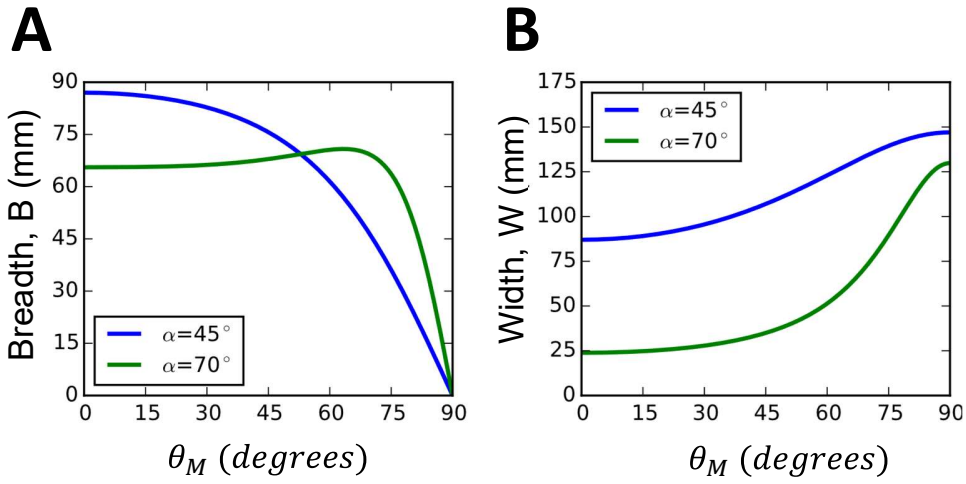

Figure 2.4: A) Breath of TMP vs θ_M; B) Width of TMP vs θ_M

70° shows the unique trend in which B decreases after a certain θ_M as it is decreased from 90° to 0°. This is unique not only because general materials show increasing breadth with decreasing height but also because of the fact that the breadth increases before decreasing after a certain θ_M. Based on this , it is understood that TMP of α - 70° will show unique response to compression loading in the breadthwise direction which can be very different from the response of TMP of α of 45°. Thus the force-displacement relations are applied to these two configurations in this research and the results are analysed to understand the difference in behaviors of these two configurations and to unravel the unique behaviors. The folding motion and various views of TMP of the two α values - 45° and 70° are shown in figure 2.5.

The geometric relations of the TMP discussed in this chapter form the basis for developing the force-displacement relations for the TMP. These are explained in the subsequent chapters.

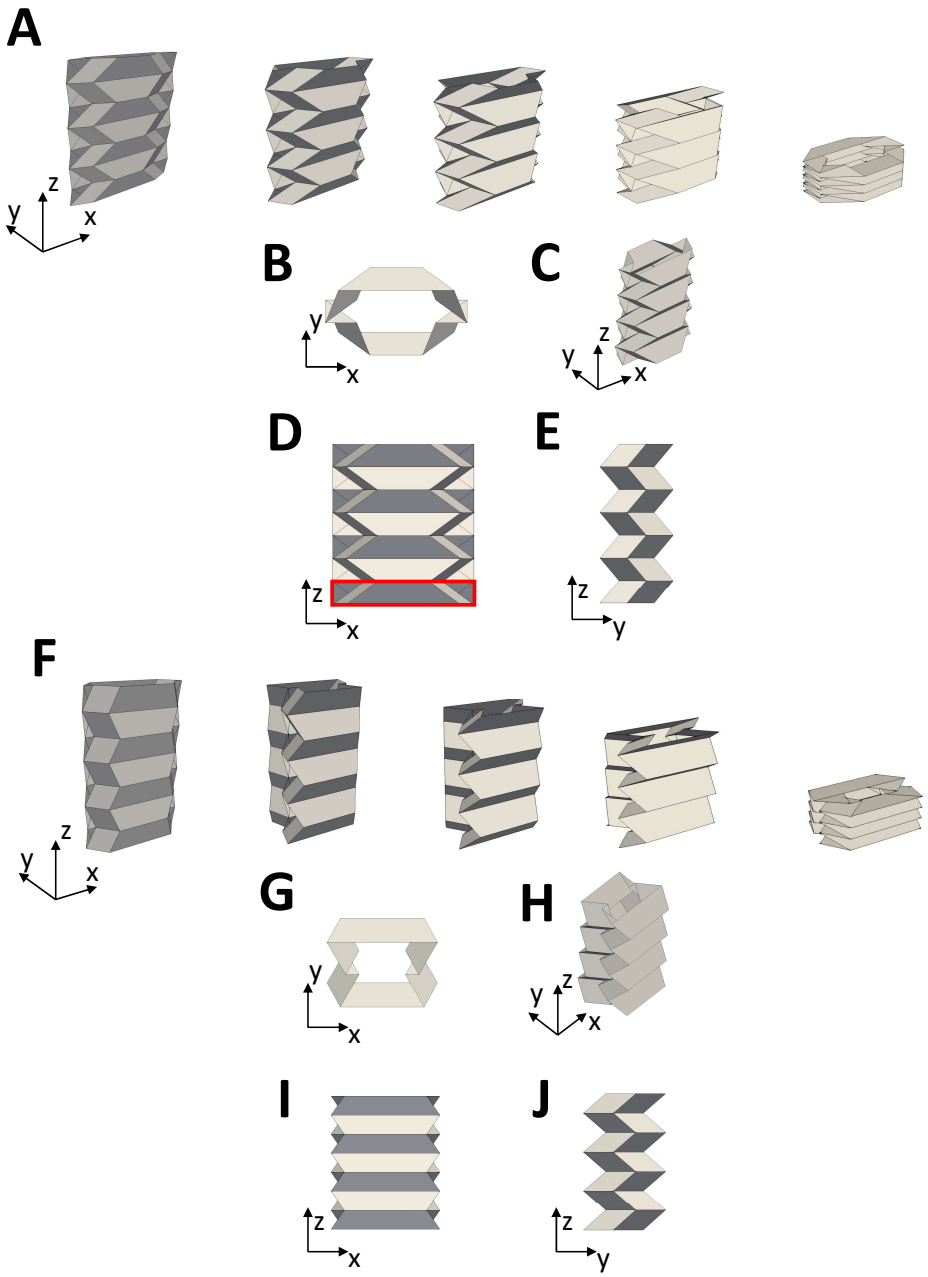

Figure 2.5: A) Folding Motion of TMP - $\alpha = 45°$ (See left to right); B) Top view of TMP - $\alpha = 45°$; C) Isometric view of TMP - $\alpha = 45°$; D) Front View of TMP - $\alpha = 45°$; The red rectangle denotes one layer of TMP; E) Side view of TMP - $\alpha = 45°$; F) Folding Motion of TMP - $\alpha = 70°$ (See left to right); G) Top view of TMP - $\alpha = 70°$; H) Isometric view of TMP - $\alpha = 70°$; I) Front View of TMP - $\alpha = 70°$; J) Side view of TMP - $\alpha = 70°$

Chapter 3

FORCE-DISPLACEMENT RELATIONS OF SINGLE TMP CELL

The major aim of this research is to understand the load carrying capability of the TMP under compression loading. For this purpose, the force-displacement relations for the structure under three directions of compression were developed. The development of these relations and the application of those to the TMP of the two configurations under consideration are discussed in detail in this chapter. The TMP has been found to exhibit simultaneous high and low load carrying capabilities under compression in one of the directions. This is also explained in detail in this chapter.

3.1 Principle of virtual work

The geometric parameters and relationships explained in previous chapter is used along with the principle of virtual work to derive the force-displacement relations for the TMP. The structure is modelled by considering the crease lines as hinged joints. The hinged joints are torsional springs which will have a finite torsional rigidity. So, the TMP is a rigid foldable origami meaning that it can be folded without deforming the facets. On applying the principle of virtual work to the TMP, it is understood that the energy for deforming the structure is equal to the energy required to surpass the torsional rigidity of the hinges. Based on this, the following relation is developed [13]:

$$F\delta u \ = 2n_M M_M \delta\theta_M + 2n_S M_S \delta\theta_S \tag{3.1}$$

where $n_M = 8(N-1)$ and $n_S = 8N$ are the number of main and sub crease lines respectively. The moment formula is given as $M = 2k_\theta\,(\theta^0 - \theta)$, where θ^0 is the initial folding

angle and k_θ is the torsional rigidity of crease [13]. Using the above expressions, the force-displacement relationship of the structure under three mutually perpendicular directions of compression loading named as axial direction, lateral direction and transverse direction are studied . The three mutually perpendicular directions of compression loading on the single TMP cell are shown in figure 3.1.

The force-displacement relation for TMP under axial direction was previously studied by our group [13]. It was found that the structure exhibited negative stiffness in axial direction. The possibility of novel behavior of TMP in the lateral and transverse directions of loading suitable for deployable and load supporting structures forms the basis for this thesis and those force-displacement relations form the crux of this work. However, all three force-displacement relations are explained in the following sections for the sake of completeness.

3.2 Force-displacement relations for single-TMP

First, the force-displacement relation of TMP under axial loading is explained. The displacement is taken to be positive in the direction of motion of the TMP under all loading conditions. Thus the downward axial direction is positive displacement for the axial compression loading and it is termed as u_1. The displacement u_1 is derived from the height H of the TMP as follows [13]:

$$\begin{aligned} H_o - u_1 &= Nd\sin\theta_M \\ u_1 &= Nd\left(\sin(\theta_M^0) - \sin\theta_M\right) \end{aligned} \tag{3.2}$$

where H_o is the initial height of the structure and u_1 is the displacement along downward axial direction due to compression. and then the δu required in the principle of virtual work is derived as derivative of u_1 as follows [13]:

$$\delta u_1 = -Nd\cos\theta_M\delta\theta_M. \tag{3.3}$$

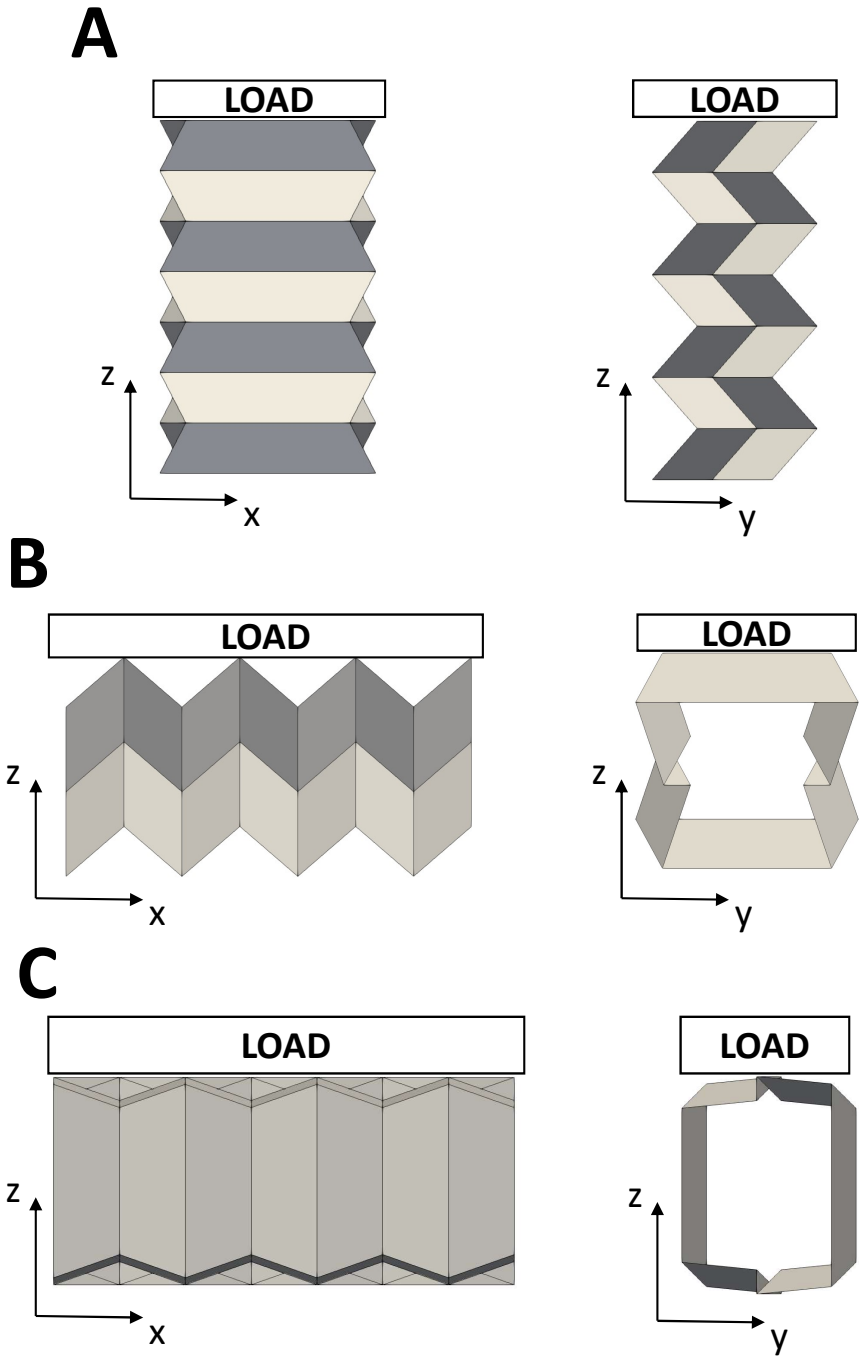

Figure 3.1: Three directions of Compression of TMP ; A) Axial Compression; B) Lateral Compression; C) Transverse Compression

Inserting the δu_1 into the principle of virtual work, we arrive at the axial compressive force-displacement relation as follows [13]:

$$\begin{aligned} F_1 \delta u_1 &= 2n_M M_M \delta\theta_M + 2n_S M_S \delta\theta_S \\ \frac{F_1}{(k_\theta/d\ )} &= -\frac{32}{\cos\theta_M}\{\frac{N-1}{N}(\theta_M - \theta_M^0) + (\theta_S - \theta_S^0)\frac{\cos^3\frac{\theta_G}{2}\sin\theta_M}{\cos\alpha\sin\theta_S}\} \end{aligned} \tag{3.4}$$

The force in the Eq.(3.4) is independent of k_θ and d as the force is normalized by the ratio of k_θ and d.

Now, the lateral loading case is considered. In this loading case, the displacement will occur in the downward breadth (i.e., B) direction of the structure and it is termed as u_2. The expression for u_2 is derived from the breadth B of the TMP as follows [14]:

$$B_o - u_2 = 2m\sin(\theta_G) + d\cos(\theta_M) \tag{3.5}$$

where B_o is the initial breadth of the structure and u_2 is the displacement along breadth-wise direction due to compression. And then corresponding δu_2 is derived as derivative of u_2 as follows [14]:

$$\begin{aligned} \delta u_2 &= -(2m\cos\theta_G)\,\delta\theta_G + (d\sin\theta_M)\,\delta\theta_M \\ \delta u_2 &= -(2m\cos\theta_G)\left(-2\tan\alpha\cos^2\frac{\theta_G}{2}\sin\theta_M\right)\delta\theta_M + (d\sin\theta_M)\,\delta\theta_M \end{aligned} \tag{3.6}$$

Inserting the δu_2 into the principle of virtual work,

$$F_2 \delta u_2 = 2n_M M_M \delta\theta_M + 2n_S M_S \delta\theta_S, \tag{3.7}$$

we arrive at the lateral compression force-displacement relation as follows [14]:

$$\begin{aligned} \frac{F_2}{(k_\theta/d\ )} = \frac{32}{\sin\theta_M\{4\,(m/d\ )\cos\theta_G\tan\alpha\cos^2(\theta_G/2\ )+1\}} \times \\ \left\{(N-1)\left(\theta_M - \theta_M^0\right) + N\left(\theta_S - \theta_S^0\right)\frac{\sin\theta_M\cos^3(\theta_G/2\ )}{\cos\alpha\sin\theta_S}\right\} \end{aligned} \tag{3.8}$$

The force in the Eq.(3.8) is independent of k_θ and d as the force is normalized by the ratio of k_θ and d.

Then the response of TMP to transverse compression loading was studied. In this case, the displacement is in the downward width (W) direction of the structure and it is termed as u_3. The expression for u_3 is derived from W of structure as follows [14]:

$$W_o - u_3 \quad = 2\left(\tfrac{d}{2\tan\alpha} + m\cos\left(\theta_G\right) + l\right) \tag{3.9}$$

where W_o is the initial width of the structure and u_3 is the displacement along widthwise direction due to compression. And then corresponding δu_3 is derived as derivative of u_3 as follows [14]:

$$\begin{aligned}
\delta u_3 &= \left(2m\sin\theta_G\right)\delta\theta_G \\
\delta u_3 &= \left(2m\sin\theta_G\right)\left(-2\tan\alpha\cos^2\frac{\theta_G}{2}\sin\theta_M\right)\delta\theta_M \\
\delta u_3 &= -4m\sin\theta_G\tan\alpha\cos^2\frac{\theta_G}{2}\sin\theta_M\delta\theta_M
\end{aligned} \tag{3.10}$$

Substituting δu_3 into the principle of virtual work,

$$F_3\delta u_3 = 2n_M M_M\delta\theta_M + 2n_S M_S\delta\theta_S \tag{3.11}$$

we arrive at the transverse compression force-displacement relation as follows [14]:

$$\frac{F_3}{(k_\theta/d\,)} = -\frac{8}{(m/d\,)\sin\theta_G}\left\{\frac{(N-1)\left(\theta_M-\theta_M^0\right)}{\tan\alpha\cos^2\left(\theta_G/2\,\right)\sin\theta_M} + \frac{N\left(\theta_S-\theta_S^0\right)\cos\left(\theta_G/2\,\right)}{\sin\alpha sin\theta_S}\right\}. \tag{3.12}$$

The force in the Eq.(3.12) is independent of k_θ and d as the force is normalized by the ratio of k_θ and d. These force-displacement relations are plotted for a set number of configurations of the TMP which represent all different possible configurations and analyzed for possible interesting behavior and also to evaluate the load carrying ability in the three directions compared to each other. This is explained in the next section.

3.2.1 Force-displacement relations for TMP of α: 45° and 70°

The force-displacement curves are valid for all configurations of TMP. The two representative configurations of TMP were identified in the last chapter and they have α of 45° and 70°.

The force-displacement curves for these two configurations with a constant set of values for the other parameters were generated. The constant set of values are as follows: $l = 40$ mm; $m = 30$ mm; $d = 30$ mm; $N = 7$. Four different initial configurations defined by 4 different θ_M^0 were considered. The force-displacement curves for the above configurations for the three directions of compression are shown in figure 3.2

All the axial force-displacement curves corresponding to $\alpha = 45°$ which are shown in part A of figure 3.2 shows monotonously increasing force-displacement behavior. It is same for all cases of $\alpha = 70°$ shown in part B of figure 3.2 except for the $\theta_M^0 = 80°$ case which shows negative stiffness behavior of the structure for a certain displacement range. In this range there is a sharp drop in the force to cause further compression which implies snap through and bistable behavior. Thus the structure can have two positions bearing the same load when $\theta_M^0 = 80°$. This is an unique behavior exhibited by only few structures.

The lateral force displacement curves for the various initial configurations of the two TMP structures are shown in parts C and D of figure 3.2. The lateral force displacement curves for all initial configurations of TMP of $\alpha = 45°$ are similar in trend to the axial force-displacement curves of TMP of $\alpha = 45°$ but it can be seen that structure can carry slightly higher load. The interesting tunable load carrying behavior is found for $\alpha = 70°$. At $\alpha = 70°$ the structure exhibits very low load carrying ability for $\theta_M^0 = 68°$ but very high load carrying ability for $\theta_M^0 = 30°, 45°$ and $60°$. Thus there is a transition point somewhere between $\theta_M^0 = 68°$ and $\theta_M^0 = 60°$, called the critical point , in which the structure transforms from low load carrying to very high load carrying behavior. Thus, if the θ_M^0 parameter of the structure can be actively controlled, tunable load carrying ability of the structure can be achieved. It was found that critical point for the configuration under consideration is $\theta_M^0 = 63°$. The configuration shows low load carrying ability for $\theta_M^0 = 64°$ and very high load carrying ability for $\theta_M^0 = 62°$. This is shown in figure 3.3. It is to be noted that the critical point is in accordance with the point where the breadth of the structure starts decreasing in the breadth vs θ_M curve shown in figure 2.4. Thus the unique trend of breadth causes the tunability of load capacity.

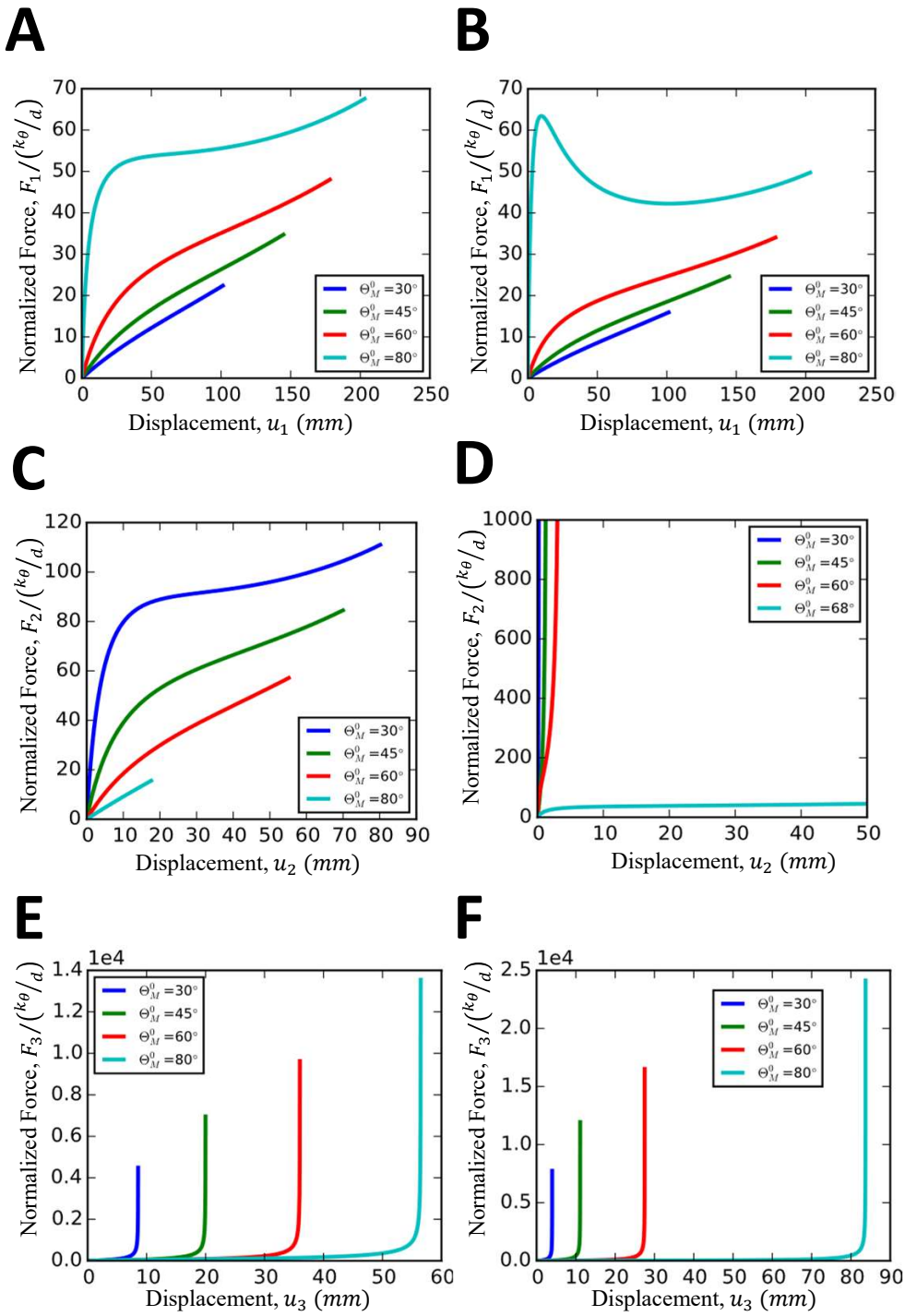

Figure 3.2: A) Axial Compression Force Displacement relation for TMP of $\alpha = 45°$; B) Axial Compression Force Displacement relation for TMP of $\alpha = 70°$; C) Lateral Compression Force Displacement relation for TMP of $\alpha = 45°$; D) Lateral Compression Force Displacement relation for TMP of $\alpha = 70°$; E) Transverse Compression Force Displacement relation for TMP of $\alpha = 45°$; F) Transverse Compression Force Displacement relation for TMP of $\alpha = 70°$

This is a novel behavior as the structure exhibits both low and high load carrying ability

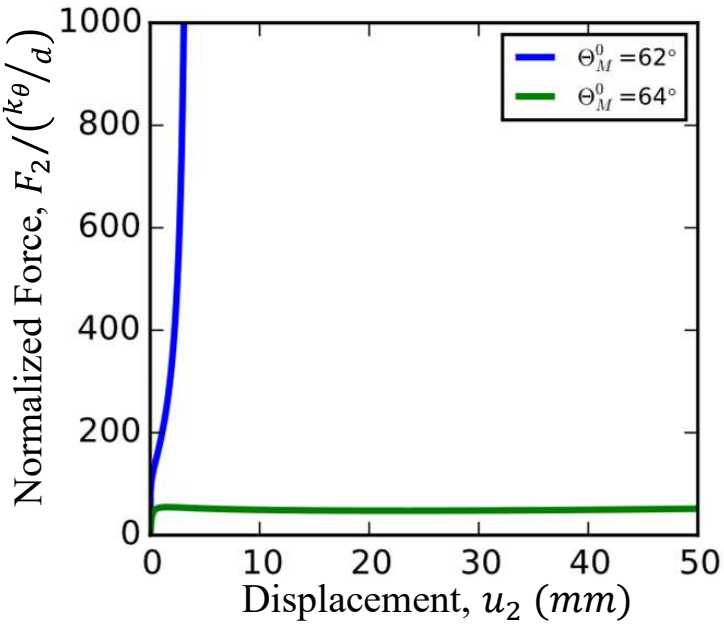

Figure 3.3: Low load-carrying and High Load-carrying configurations of TMP of $\alpha = 70°$ under Lateral Compression. $\theta_M^0 = 64°$ has low load capacity and $\theta_M^0 = 62°$ has high load capacity

with the same geometric configuration just by changing the initial position slightly. If the initial position is tuned , the behavior of structure can be tuned and we understand from the analytical relation that the structure exhibits tunable load carrying capacity under lateral compression.

The transverse force-displacement curves for TMP of α: 45° and 70° are shown in parts E and F of figure 3.2 respectively. It is observed that the transverse compression force required to fold the structure increases in the same manner for all configurations and the structure reaches a point in all configurations where the load to further compress the structure increases drastically. This implies that the structure will exhibit highly rigid behavior under transverse compression after a point and will be able to support a heavy load.

Thus, TMP of all α configurations which represent the $\alpha = 45°$ case will have much lower

load carrying capacity in axial and lateral directions compared to the transverse direction. All TMP similar to the $\alpha = 70^\circ$ case will be having lower load carrying capacity in axial compared to the transverse direction while having tunable load capacity in the lateral compression. This also implies that the structure exhibits anisotropicity. This is mathematically shown using the stiffness relations in the following section.

3.3 Anisotropicity

Stiffness of the structure is computed as the derivative of force with respect to displacement and the formulae is as below in eq.(3.13)

$$\begin{aligned}
\frac{dF}{du} &= \frac{dF/d\theta_M}{du/d\theta_M} \\
\frac{dF}{d\theta_M} &= \frac{\partial F}{\partial \theta_M} + \frac{\partial F}{\partial \theta_G}.\frac{\partial \theta_G}{\partial \theta_M} + \frac{\partial F}{\partial \theta_S}.\frac{\partial \theta_S}{\partial \theta_M} + \frac{\partial F}{\partial \delta u}.\frac{\partial \delta u}{\partial \theta_M} + \frac{\partial F}{\partial \delta u}.\frac{\partial \delta u}{\partial \theta_G}.\frac{\partial \theta_G}{\partial \theta_M} + \frac{\partial F}{\partial \delta u}.\frac{\partial \delta u}{\partial \theta_S}.\frac{\partial \theta_S}{\partial \theta_M} \\
\frac{du}{d\theta_M} &= \frac{\partial u}{\partial \theta_M} + \frac{\partial u}{\partial \theta_G}.\frac{\partial \theta_G}{\partial \theta_M} + \frac{\partial u}{\partial \theta_S}.\frac{\partial \theta_S}{\partial \theta_M}
\end{aligned} \tag{3.13}$$

The above derivatives are computed for the force-displacement relations of all three directions of loading. The analytical stiffness relations are computed for the whole range of initial configurations, each of which is characterized by a distinct θ_M^0, in each loading direction for TMP of configuration: $l = 40$ mm; $m = 30$ mm; $d = 30$ mm; $\alpha = 70^\circ$; $N = 7$. Figure 3.4 shows the analytical stiffness of the three loading directions plotted for all initial configurations of the TMP. It can be seen that for all initial configurations, i.e. θ_M^0, the stiffnesses in the three loading directions are different. However, for initial configurations between $\theta_M^0 = 65^\circ \; and \; 70^\circ$, the stiffness in the three directions are quite close to each other .Thus it can be concluded that the structure exhibits tunable anisotropic behavior meaning that the initial position can be controlled to achieve varying degree of anisotropic stiffness. This can be another feature which can be of great help for deployable structure applications.

It can be seen that the stiffness goes to infinity under lateral compression at $\theta_M^0 = 63^\circ$ which is the critical folding angle. This implies that it is not possible to transit from foldable

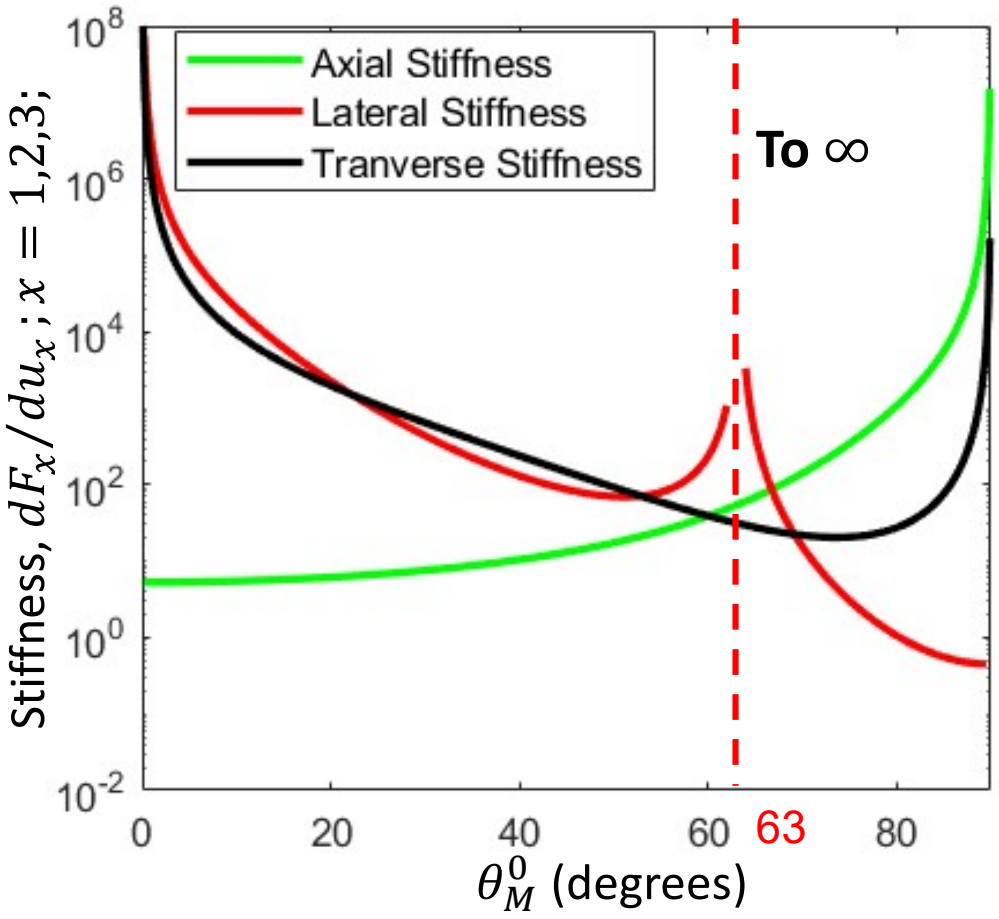

Figure 3.4: Analytical Stiffness of TMP in three directions of loading, showing tunable Anisotropicity

to rigid configuration through lateral compression thus eliminating the risk of failure under loading.

Thus it is understood mathematically that the TMP structure shows anisotropic stiffness. The structure is also found to show tunable load capacity under lateral compression. These properties make the structure perfect for deployable yet load supporting structures. These behaviors are demonstrated using paper prototypes and the mathematical relations are verified experimentally in the next chapter.

Chapter 4

EXPERIMENTAL VERIFICATION

With the force-displacement relations established mathematically, it was verified experimentally using paper prototypes. As part of this, a demonstration of the tunable load capacity and anisotropic behavior is shown using the paper prototypes. Then, compression load tests were conducted on the 3 mutually perpendicular directions on the paper TMP. The aim of conducting these experiments is to verify and validate the analytical force-displacement relations.

4.1 Demonstration using paper prototype

Here the load carrying capacities in the three directions are demonstrated on paper prototypes. To closely represent the analytical model described in previous chapter, a paper prototype has been designed and developed. As per the analytical model, the facets must be rigid while the crease lines act as torsional hinge joints. The facets should not deform during the compression of TMP. The paper prototype was constructed by cutting out specially designed crease line patterns using LASER Cutter from two flat sheets of paper and later sticking those two papers together. The design of the crease lines ensures that the prototype behaves in a rigid foldable manner closely representing the analytical model.

The paper prototypes of $\alpha = 45^\circ$ and $\alpha = 70^\circ$ are shown in figure 4.1.

We have seen from the previous chapter that TMP of $\alpha = 70^\circ$ must have high load carrying capacity in transverse direction and very low load carrying ability in the axial direction while having tunable load carrying capacity in the lateral direction. This is the unique behavior of the structure and so this has been demonstrated in figure 4.2.

It can be seen that the TMP doesn't support weight in axial direction while doing so

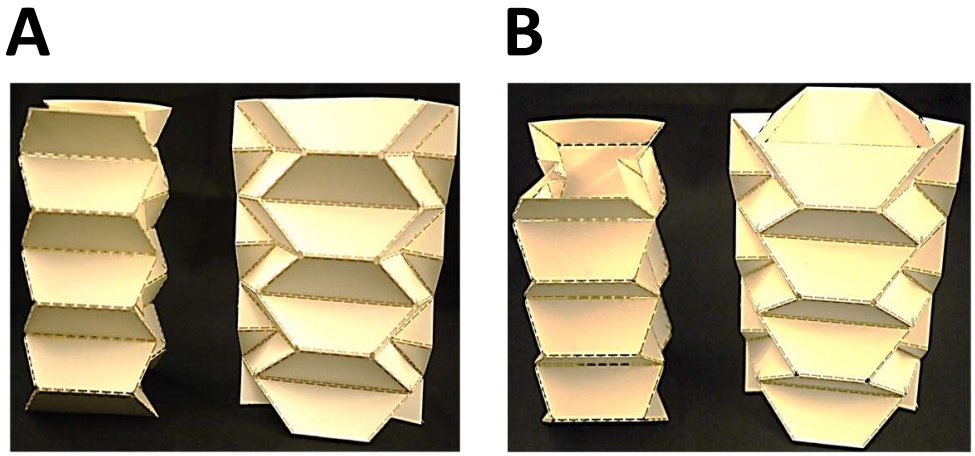

Figure 4.1: Paper Prototypes.In each picture, Left side is $\alpha = 70°$ and right side is $\alpha = 45°$. A) Front view of Prototypes and B) Isometric view of Prototypes

in the transverse direction. It can also be seen that in the lateral direction, the structure carries load for some configurations while failing to do so for some other configurations thus proving the tunability of load capacity. This indeed is a very interesting behavior and this will enable the structure to be deployable and support load on its own, thereby proving to be an effective option for the quest of deployable and load supporting structure. The anisotropic behavior of the structure is also showcased by this demonstration.

4.2 TMP compression experiments

Following the demonstration, compression experiments are carried out on TMP to obtain experimental force-displacement curves for the three mutually perpendicular directions of loading. To compare the experimental results with the analytical relations, the spring constant for the TMP crease lines is required . This is obtained by conducting single crease line compression tests.

By plugging in the experimentally determined spring constant values into the analytical relations, comparison between experimental curves and analytical relations is made. The

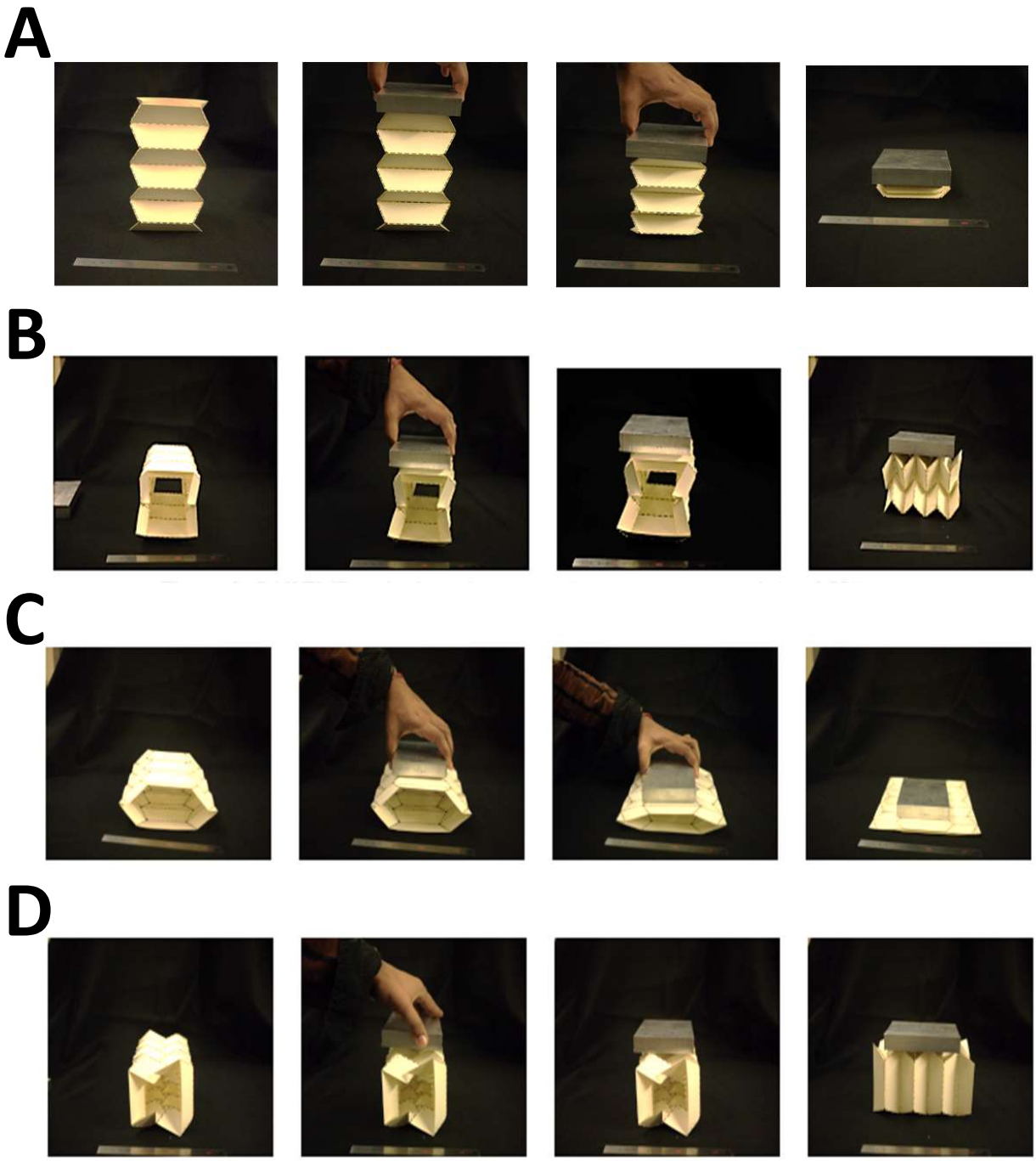

Figure 4.2: TMP Paper prototype loaded in three directions; A) Low load carrying capacity under Axial compression;B)The weight supported by TMP in one of its high load carrying configurations in Lateral compression; C)The weight NOT supported by TMP in one of its low load carrying configurations in Lateral compression;D)The weight supported by TMP under Transverse compression; This is a modified version of an image in [14]

details are explained in the following sections.

4.2.1 TMP compression tests - setup and methodology

The test setup consists of a stepper motor driven lead screw which drives the compression plate up and down. The compression plate is attached to a load cell (LUX-B-50N-ID, Kyowa) to measure the compression force. The displacement of the compression platen is calculated from the velocity of the platen which is given by the sensor within the motor. The motor is controlled to drive the lead screw at a constant velocity.

The compression platen is a flat uniform acrylic plate as shown in figure 4.3. This is to ensure, uniform loading of the TMP to closely represent the analytical model. The compression platen had to be supported by two rods to ensure it did not become inclined. The support rods are also shown in the figure 4.3. Unfortunately, the support rods added friction and bought more work to be done.

The effect of friction was deducted from the force-displacement curves obtained from the experiments. Before the start of the experiment, the rods were lubricated and then the compression platen was driven up and down with no load except the friction of the lubricated support rods. This was done 3 times to stabilize the frictional resistance. Then, compression tests were conducted.

During the compression test, the paper prototype was first set to the required initial configuration. Then the prototype at the required initial configuration was compressed under the test setup. This process was repeated 3 times, each time with the same initial configuration. Finally to find the frictional resistance offered by the support rods during the tests, the compression platen was again driven up and down with just the support rods on but this time, the force and displacement were recorded. This was also repeated 3 times.

The force output of load cell during the compression test on TMP is called the total force as it is combination of both TMP compression force and support rod frictional resistance. The force output of load cell during the tests with only support rods is called frictional force. Average of the total force and frictional force were determined and then, the average

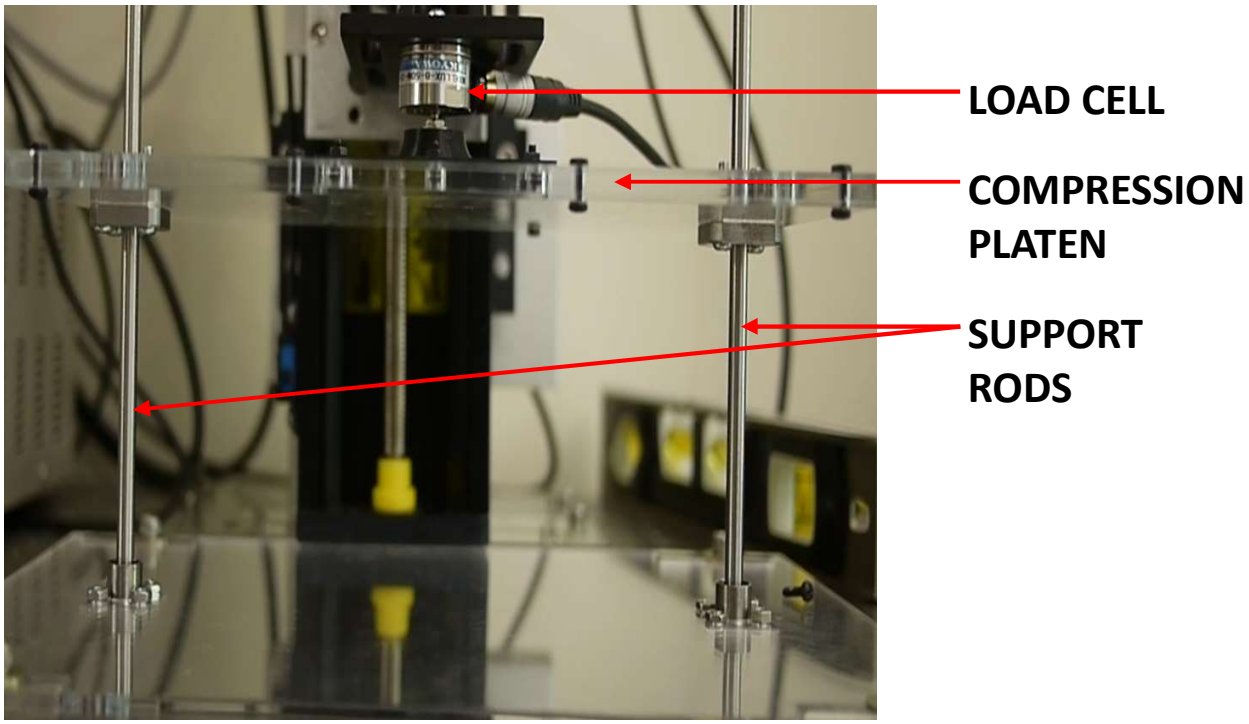

Figure 4.3: Experimental setup for TMP Compression test

frictional force was deducted from the average total force which gave the average compression force. This is depicted in figure 4.4.

This procedure was carried out in the three mutually perpendicular directions. The

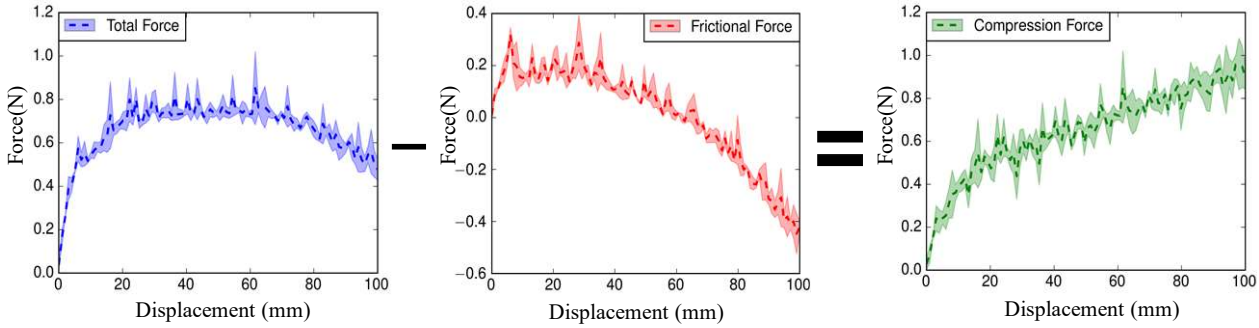

Figure 4.4: Deduction of Frictional Force effects

results are explained in the following section.

4.2.2 Spring constant determination tests - setup and methodology

Then, as previously mentioned, the spring constant of crease line of the TMP had to be determined to compare the experimental results with the analytical results. This test was done in similar manner to a test done previously [15]. The single crease specimen was fabricated in the same manner as the paper TMP and a special fixture was designed to ensure that the specimen behaves in a rigid foldable manner. The fixture for the spring constant test is shown in figure 4.5.

The spring constant was determined from the force-displacement results of the experiment by applying the formula for moment to compress a torsional spring . The formula applied to determine the spring constant is as follows:

$$\begin{aligned} M &= 2k_\theta \left(\theta_M - \theta_M^0\right) W \\ k_\theta &= \frac{M}{2W\left(\theta_M - \theta_M^0\right)} = \frac{FL\cos\theta_M}{2W\left(\theta_M - \theta_M^0\right)} \end{aligned} \tag{4.1}$$

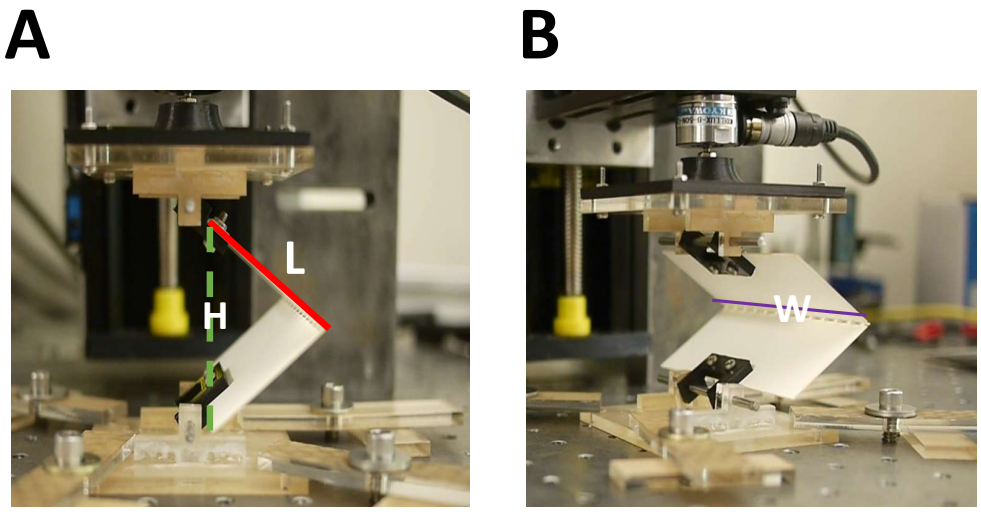

Figure 4.5: Test Setup for Spring Constant k_θ Determination

where

$$\theta_M = \sin^{-1}\left(\frac{H}{2L}\right)$$
$$\theta_M^0 = \sin^{-1}\left(\frac{H_o}{2L}\right) \tag{4.2}$$

where

W = Width of Single crease line

L = Length of one facet of specimen

H = Vertical height from top to bottom corners of the specimen

H_o = Initial vertical height from top to bottom corners of the specimen

In the test, single crease specimens were compressed about 10 times by hand before the test to make it closely represent the TMP that was tested. The TMP creases would be compressed about 10 times before the test while fabricating it as well as while setting the initial position. Then the seasoned single crease specimens were compressed in the compression tester. The tests were carried out 5 times for 3 different H_o values.

The above equation (4.1) was fitted to the single crease specimen force-displacement results and the spring constant was determined as average of fits of five test results. It was

found to be 0.022 [N/(mm-rad)]. The spring constant was found to be invariant with H_o and thus can be considered as constant for a prototype of a given material configuration.

The spring constant value determined experimentally was plugged into the analytical relations and then the analytical relations were compared with the experimental results. The comparison is shown in the following section.

4.3 Experimental results

4.3.1 Axial compression results

Axial compression was performed on a paper prototype with the following geometric configuration: $l = 40$ mm ; $m = 30$ mm ; $d = 30$ mm ; $\alpha = 65°$; $\theta_M^0 = 59°$; $N = 7$; The experimental results compared with analytical relation for axial compression is shown in Figure 4.6.

It can be seen that the experiments correlate pretty closely with the analytical relation for axial compression. The analytical relation seem to be underpredicting the experiment but when the spring constant was arbitrarily increased to 0.03 [N/mm-rad], the two curves lay on top of each other. Thus the variation is actually brought in by the difference in the condition of the single crease used in the spring constant test compared to the crease condition in the TMP that was tested. The structure can carry about 1N under axial compression.

4.3.2 Lateral compression results

For lateral compression, it is understood that the structure exhibits very high load carrying capacity for some configurations and very low load capacity for some other configurations. Thus experiments were conducted on a configuration of both kinds. The high load capacity configuration is as follows: $l = 30$ mm ; $m = 30$ mm ; $d = 27$ mm ; $\alpha = 65°$; $\theta_M^0 = 49°$; $N = 7$;

The low load carrying capacity configuration is as follows: $l = 30$ mm ; $m = 30$ mm ; $d = 27$ mm ; $\alpha = 65°$; $\theta_M^0 = 64°$; $N = 7$; The experimental results compared with

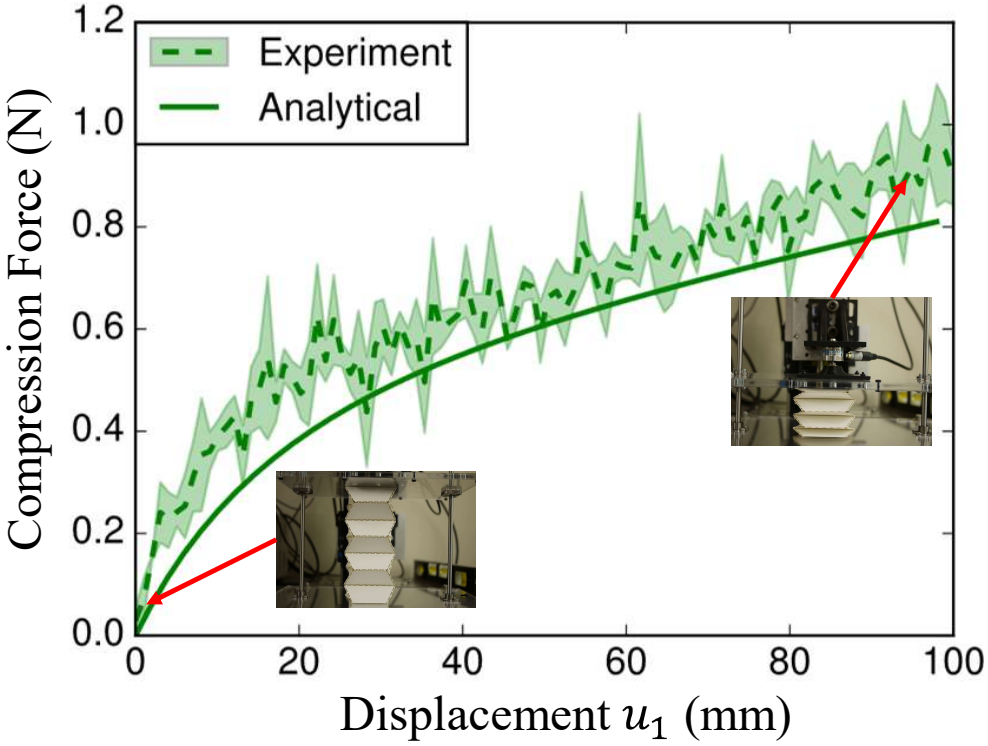

Figure 4.6: Comparison between Experimental Results and Analytical Relations for Axial Compression

analytical relation for lateral compression of high and low load capacity configuration is shown in Figure 4.7. The high load capacity configuration is called as "highly rigid" and low load capacity configuration is called as "flat foldable" in the plot.

It can be seen from figure 4.7 that the structure has been experimentally proven to exhibit tunable load capacity behavior. The high load capacity configuration carries higher than 10 times the load carried by the low load capacity configuration with much lower displacement. The experimental results are in close accordance with the analytical results in the early stages but there is increasing variation between the two as displacement increases. The reason for the variation in the high load capacity configuration is that the structure's facets begin to behave as deformable bodies beyond a particular force thus breaking the rigid origami assumption. The reason for the variation in the low load configuration was found to be the frictional effects from the base plate on which the TMP rests. The analytical relation doesn't take friction into account. Thus the analytical relations for the lateral compression are valid only upto certain load. Nevertheless, the trends are same and the structure still possess the tunable load capacity as suggested by the analytical relations.

4.3.3 Transverse compression results

Transverse compression was performed on a paper prototype with the following geometric configuration: $l = 30$ mm ; $m = 25$ mm ; $d = 43$ mm ; $\alpha = 45^\circ$; $\theta_M^0 = 60^\circ$; $N = 5$; The experimental results compared with analytical relation for transverse compression is shown in Figure 4.8.

It can be seen that the correlation between experiments and the analytical relation for transverse compression is pretty similar to that of axial compression. The reasons for the variation in this case are both the difference in condition of single crease specimens and also the frictional effects from base plate. Thus another term to account for friction in the analytical relations will improve the prediction. It has been proved that the structure exhibits high load carrying capability in the transverse direction and it supports about 10 times more load than axial direction and lateral-low load capacity configuration with lower displacement.

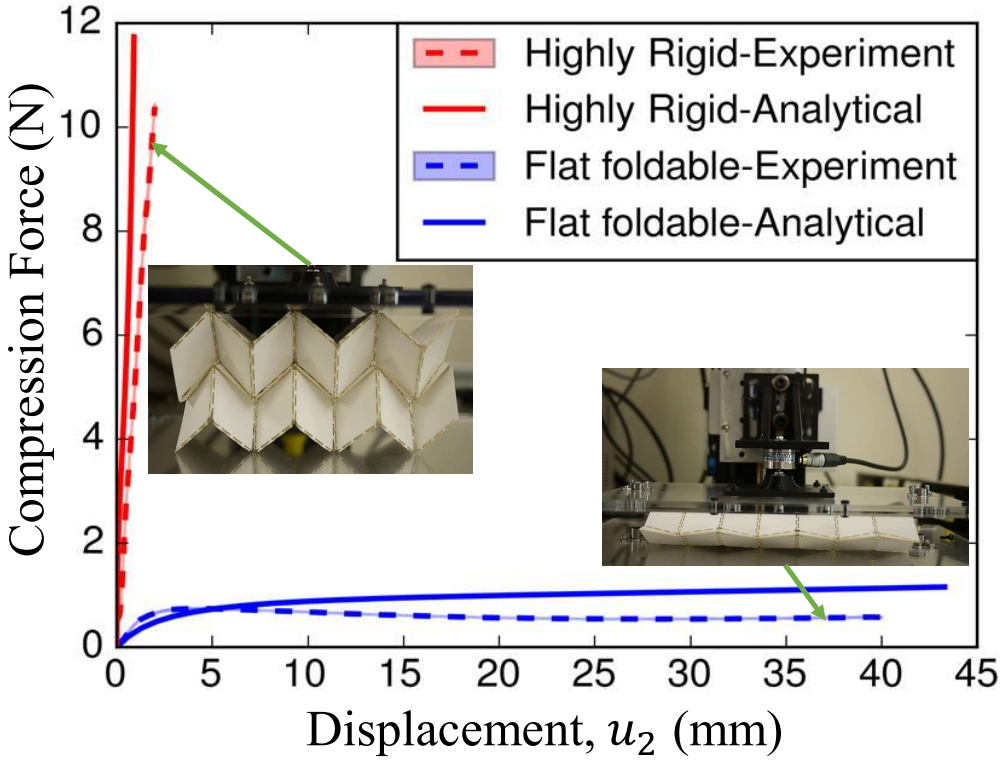

Figure 4.7: Comparison between Experimental Results and Analytical Relations for Lateral Compression

Thus the analytical relations for the TMP under three mutually perpendicular directions

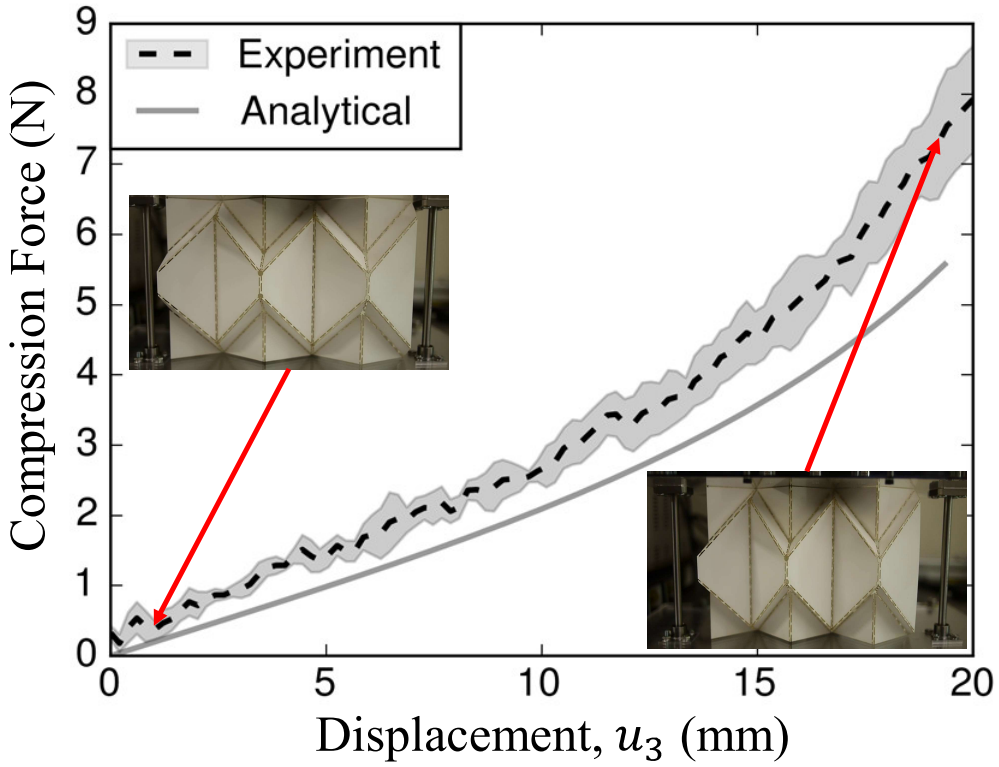

Figure 4.8: Comparison between Experimental Results and Analytical Relations for Transverse Compression

of loading has been verified experimentally and they are found to work good to predict the behavior of structure under static compression loading eventhough there are small variations between experimental result and analytical relation. The reasons for variation are explained and a better model shall be developed in the future. More importantly, the load capacity in the three directions are found to be in accordance with the prediction as in whether it is high or low. The tunable load capacity in the lateral compression is observed cleanly. Now, the same relations can be extended to predict the behavior of a multi-TMP structure which is a combination of many single TMP cells. This is explained in detail in the next chapter.

Chapter 5

MULTI-TMP STRUCTURE

The TMP structure is indeed a novel structure exhibiting unique behavior. It can be the answer for the need for space saving structures in this world which faces an ever-increasing population as well as for need for deployable structures for space applications. The TMP can be a better fit for these applications if they are stacked together in certain configurations thereby forming what are called multi-TMP structures.

The multi-TMP structures can be developed by stacking the single unit cells together and there are many different ways to do it. One such combination has been studied as part of this research. The combination is shown for $\alpha = 45°$ unit cells in figure 5.1 and for $\alpha = 70°$ unit cells in figure 5.2.

For this combination, the number of unit cells in all rows are same and number of unit cells in all columns are same.

5.1 Geometry of multi-TMP

The geometry of the multi-TMP structure can be characterized by addition of 2 new terms called N_B and N_W . N_B is the number of unit cells in one edge along the breadth direction of multi-TMP . N_W is the number of unit cells in one edge along the width direction of multi-TMP. For instance, for the multi-TMP shown in figure 5.3, N_B is 4 and N_W is 5.

The total number of unit cells in the multi-TMP structure will be $N_B * N_W$ and it is called as P. Now for the configuration shown in figure 5.3, the breadth, height and width are derived from the breadth, width and height of unit cells with the use of N_B and N_W .

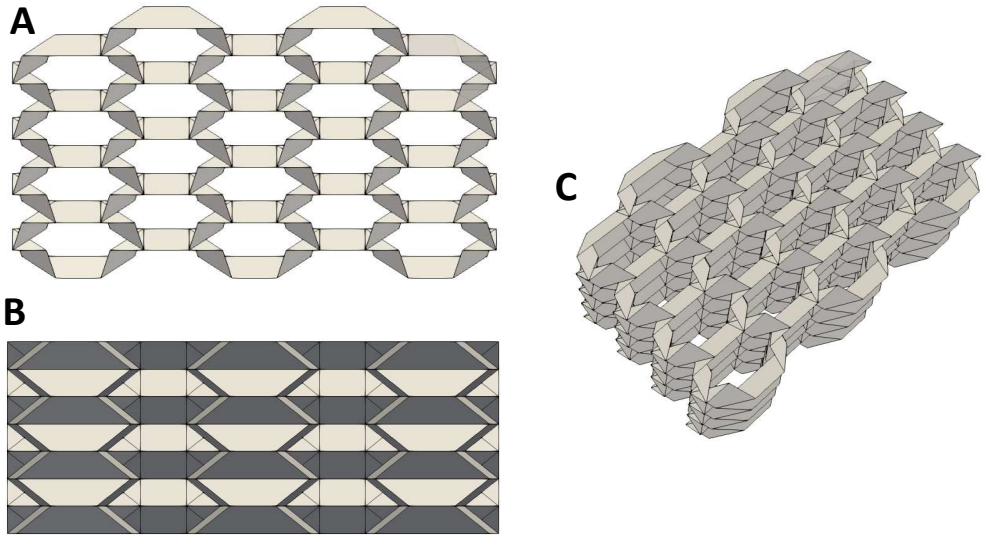

Figure 5.1: multi-TMP structure with TMP unit cells of $\alpha = 45°$; A) Top View; B) Front View; C) Isometric view

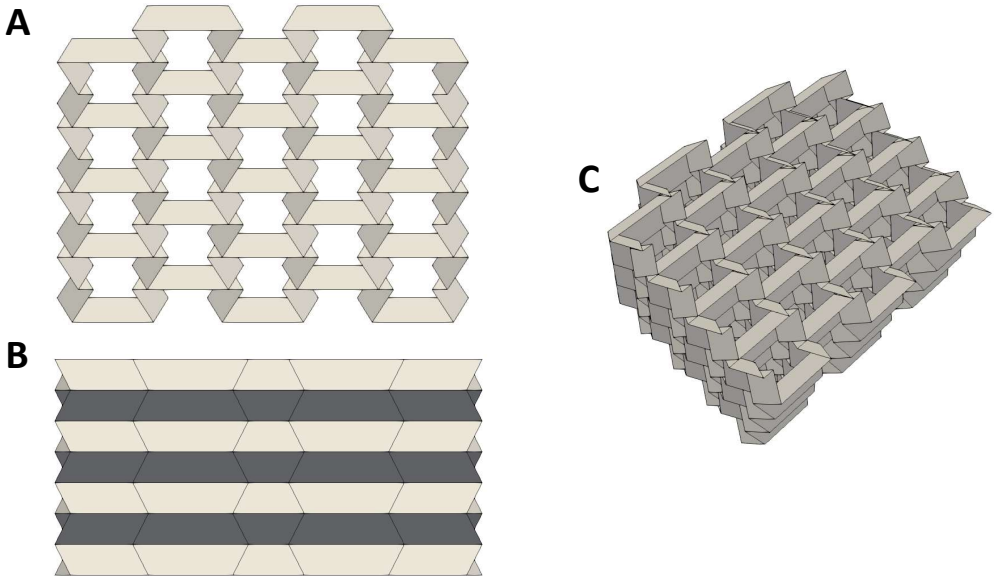

Figure 5.2: multi-TMP structure with TMP unit cells of $\alpha = 70°$; A) Top View; B) Front View; C) Isometric view

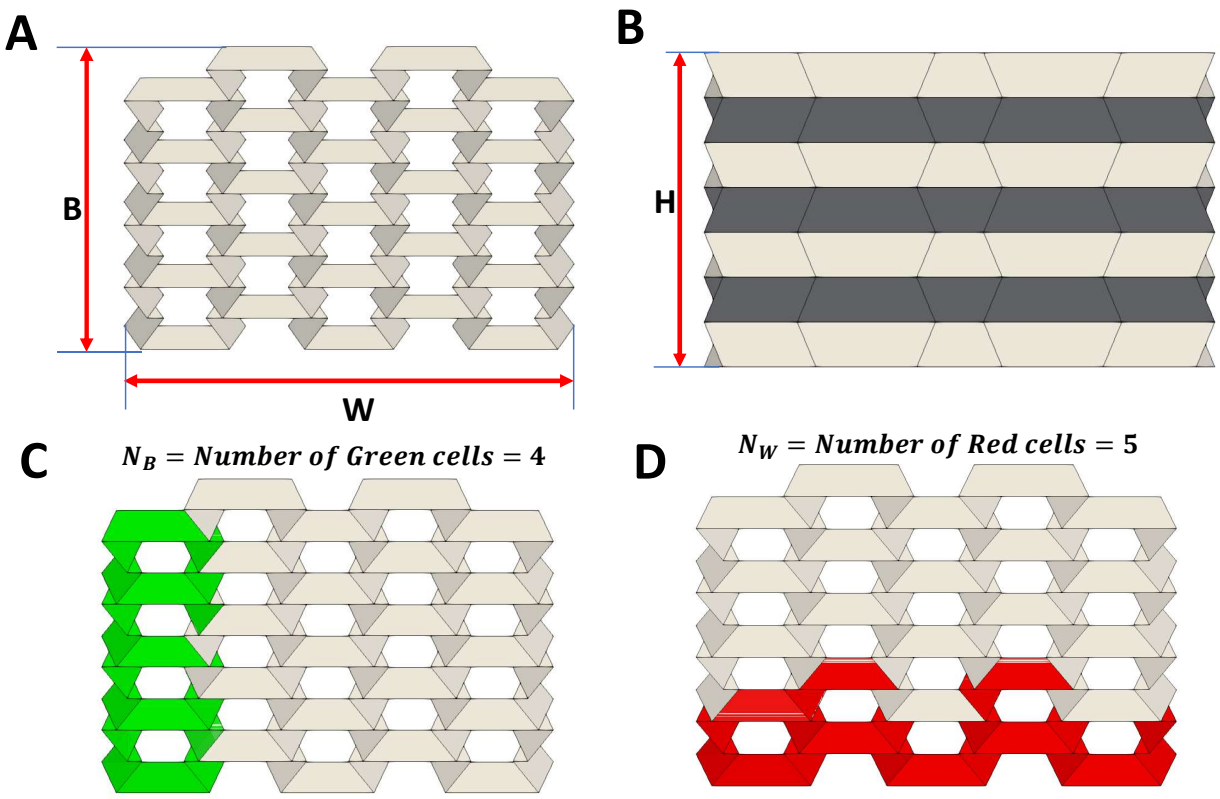

Figure 5.3: Geometry of multi-TMP structure; A) Top view of multi-TMP structure showing its Breadth,B and Width,W; B) Side view of multi-TMP showing the Height,H of the structure; C) Top view of structure showing N_B; D) Top view of structure showing N_W

The expressions are as follows:

$$\begin{aligned} B &= 1.5(2m\sin\theta_G + 0.66d\cos\theta_M) + (N_B - 1)(2m\sin\theta_G) \\ W &= (2l + \frac{d}{\tan\alpha} + 2m\cos\theta_G) + (N_W - 1)(2l + \frac{d}{2\tan\alpha} + m\cos\theta_G) \\ H &= Nd\sin\theta_M \end{aligned} \tag{5.1}$$

Another interesting geometric property of multi cellular structures is Relative Density. Relative density is defined as the ratio of density of the structure to the density of the solid that makes up the structure [16]. This translates as ratio of volume of solid to volume of structure. The volume ratio is found by considering the unit cell. The volume of structure is calculated as cross-sectional area multiplied by height of unit cell. This is shown in Eq.(5.2) below:

$$\begin{aligned} A &= 2m\sin\theta_G(2l + m\cos\theta_G) \\ V_S &= 2md\sin\theta_M\sin\theta_G(2l + m\cos\theta_G) \end{aligned} \tag{5.2}$$

Next, the volume of solid is calculated as area of the sheets of paper which make up the unit cell multiplied by the thickness of the paper. This volume is divided by two as each sheet of paper is shared by 2 unit cells in a multi-TMP structure.

$$\begin{aligned} V^* &= (Area\ of\ front\ and\ back\ sheets) \times t \times \frac{1}{2} \\ &= td\{2(l+m) + \frac{d}{2\tan\alpha}\} \end{aligned} \tag{5.3}$$

The ratio of the volumes is shown in Eq.(5.4) and it is the relative density of the multi-TMP.

$$\frac{\rho^*}{\rho} = \frac{t}{m}\frac{2(l+m) + d/(2\tan\alpha)}{2\sin\theta_M\sin\theta_G(2l + m\cos\theta_G)} \tag{5.4}$$

It is plotted for various main folding angles θ_M for three α values of $30°, 45°\ and\ 70°$ and it is shown in figure 5.4. It is seen that relative density is equal to 1 almost near the two extreme values of the main folding angle θ_M. In between these two extremes, the relative density goes to a minimum of about 0.02 for the three α configurations. Thus, the density of

the structure can be tuned to be very close to that of the solid or to be very small compared to that of the solid as the application demands.

The geometric relations above are used to extend the force-displacement relations of

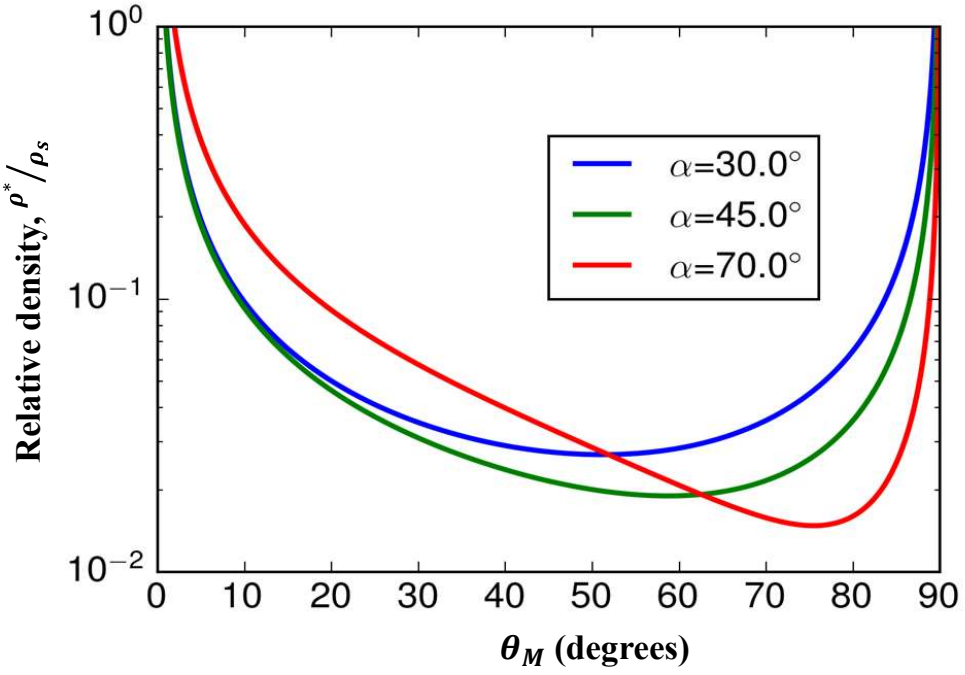

Figure 5.4: Relative Density vs θ_M for the multiTMP of various α values

the single-TMP structure to the multi-TMP structure and they are explained in the next section.

5.2 Force-displacement relations

5.2.1 Principle of Virtual Work

The same three perpendicular directions of loading as the single TMP are considered for the multi TMP as well. The three directions of loading for the multi-TMP are as shown in figure 5.5.

The same principle of virtual work is applied to the multi-TMP and it is shown in

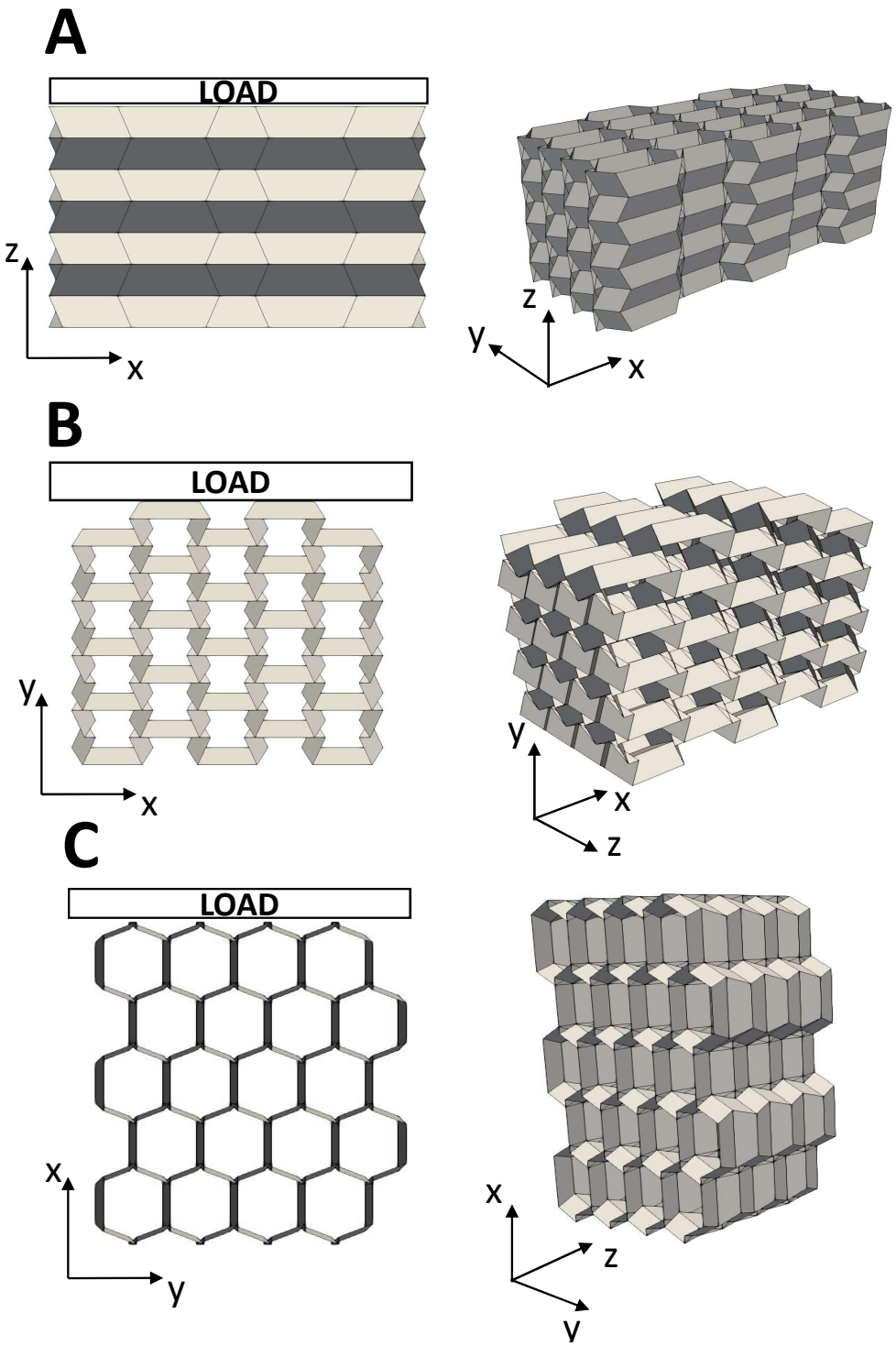

Figure 5.5: Three directions of Compression of multi TMP; A) Axial Compression; B) Lateral Compression; C) Transverse Compression

eq.(5.5) below:

$$F\delta u = -4k_\theta((\theta_M - {\theta_M}^0)L_M + L_S(\theta_S - {\theta_S}^0)\frac{\sin\theta_M \cos^3(\theta_G/2)}{\cos\alpha \sin\theta_S}) \tag{5.5}$$

Where

k_θ=Spring constant per unit length of crease line

L_M=Total length of main crease lines

L_S=Total length of sub crease lines

The L_M and L_S are derived as follows:

Total number of Main and Sub crease lines in a layer of TMP = 8

Therefore, Length of a Main crease line,

$$l_M = \frac{4l + 4m + \frac{2d}{\tan\alpha}}{8} = \frac{l + m + \frac{d}{2\tan\alpha}}{2} \tag{5.6}$$

Length of a sub crease line,

$$l_S = \frac{d}{\sin\alpha} \tag{5.7}$$

It is to be noted that all the crease lines except for those at the boundaries are shared by two TMP unit cells in the multi-TMP configuration. Based on this, the total length of main and sub creases can be found from length of single main- and sub-crease as follows:

Total number of shared main crease lines =$P(4(N-1))$

Total length of shared main crease lines = $Pl_m(4(N-1))$

Length of unshared main crease along Width direction $L_W = N_W(N-1)(2l+m+\frac{d}{2\tan\alpha})$

Length of unshared main creases along Breadth direction:

If N_B is even, $L_B = (N_B+1)(m+d)(N-1)$

If N_B is odd, $L_B = (N_B+2)(m+d)(N-1)$

$\implies$ Total length of Main crease lines,$L_M = Pl_m(4(N-1)) + L_W + L_B$

Total number of shared sub creases = $P(4N)$

Total number of unshared sub creases in width direction = $(2N_W - 2)N$

Total number of unshared sub creases in breadth direction = $4N_B(N)$

$\implies$ Total length of Sub Crease lines, $L_S = (P + N_B + \frac{N_W}{2} - \frac{1}{2})(4N)l_S$

The L_M and L_S are plugged into principle of virtual work to derive force displacement relations for three directions of loading of multi-TMP. The notations for the displacement and force in various loading directions are same as the single TMP structure.

5.2.2 Force Displacement Relations

First, the axial compression direction is considered. The expression for displacement u_1 is derived from height H of the structure as shown in eq.(5.8) below:

$$\begin{aligned} H_o - u_1 &= Nd\sin\theta_M \\ u_1 &= Nd(\sin(\theta_M^0) - \sin\theta_M) \end{aligned} \tag{5.8}$$

δu_1 is derived from u_1 as follows:

$$\delta u_1 = -Nd\cos\theta_M\delta\theta_M \tag{5.9}$$

The δu_1 is plugged into the principle of virtual work in eq.(5.5) and the normalized force-displacement relation of multi-TMP under axial compression is derived. It is shown in eq.(5.10) below:

$$\frac{F_1}{k_\theta/d} = \frac{-4((\theta_M - {\theta_M}^0)L_M + L_S(\theta_S - {\theta_S}^0)\frac{\sin\theta_M\cos^3(\theta_G/2)}{\cos\alpha\sin\theta_S})}{N\cos\theta_M} \tag{5.10}$$

The force in the Eq.(5.10) is the force normalized by the ratio of k_θ and d, thus giving a relation independent of k_θ and d.

Next, the lateral compression direction is considered. The expression for displacement u_2 is derived from breadth B of the structure as shown in eq.(5.11) below:

$$B_o - u_2 = 1.5(2m\sin\theta_G + 0.66d\cos\theta_M) + (N_B - 1)(2m\sin\theta_G) \tag{5.11}$$

δu_2 is derived from u_2 as follows:

$$\begin{aligned} \delta u_2 &= -3m\cos\theta_G\delta\theta_G + d\sin\theta_M\delta\theta_M - (N_B - 1)(2m\cos\theta_G\delta\theta_G) \\ \delta u_2 &= ((3m + 2m(N_B - 1))(\cos\theta_G)(2\tan\alpha\cos^2\frac{\theta_G}{2}\sin\theta_M) + d\sin\theta_M)\delta\theta_M \end{aligned} \tag{5.12}$$

The δu_2 is plugged into the principle of virtual work in eq.(5.5) and the normalized force-displacement relation of multi-TMP under lateral compression is derived. It is shown in eq.(5.13) below:

$$\frac{F_2}{k_\theta/d} = \frac{4((\theta_M - {\theta_M}^0)L_M + L_S(\theta_S - {\theta_S}^0)\frac{\sin\theta_M \cos^3(\theta_G/2)}{\cos\alpha \sin\theta_S})}{((3(m/d) \ + 2(m/d\,)(N_B - 1))(\cos\theta_G)(2\tan\alpha\cos^2\frac{\theta_G}{2}\sin\theta_M) + \sin\theta_M)} \tag{5.13}$$

The force in the Eq.(5.13) is the force normalized by the ratio of k_θ and d, thus giving a relation independent of k_θ and d.

Finally, the transverse compression direction is considered. The expression for displacement u_3 is derived from the width W of structure as shown in eq.(5.14) below:

$$W_o - u_3 = (2l + \frac{d}{\tan\alpha} + 2m\cos\theta_G) + (N_W - 1)(2l + \frac{d}{2\tan\alpha} + m\cos\theta_G) \tag{5.14}$$

δu_3 is derived from u_3 as follows:

$$\begin{aligned}
\delta u_3 &= (N_W + 1)(m\sin\theta_G \delta\theta_G) \\
\delta u_3 &= (N_W + 1)(m\sin\theta_G(-2\tan\alpha\cos^2\frac{\theta_G}{2}\sin\theta_M))\delta\theta_M \\
\delta u_3 &= -(N_W + 1)(2m\sin\theta_G\tan\alpha\cos^2\frac{\theta_G}{2}\sin\theta_M)\delta\theta_M
\end{aligned} \tag{5.15}$$

The δu_3 is plugged into the principle of virtual work in eq.(5.5) and the force-displacement relation of multi-TMP under transverse compression is derived. It is shown in eq.(5.16) below:

$$\frac{F_3}{k_\theta/d} = \frac{-4((\theta_M - {\theta_M}^0)L_M + L_S(\theta_S - {\theta_S}^0)\frac{\sin\theta_M \cos^3(\theta_G/2)}{\cos\alpha \sin\theta_S})}{(N_W + 1)(2\,(m/d\,)\sin\theta_G\tan\alpha\cos^2\frac{\theta_G}{2}\sin\theta_M)} \tag{5.16}$$

The force in the Eq.(5.16) is the force normalized by the ratio of k_θ and d, thus giving a relation independent of k_θ and d. Similar to the single-TMP, these force-displacement relations are plotted for a set number of configurations of the multi-TMP to see if the multi-TMP exhibits similar behavior in terms of load capacity. This is explained in the next section.

5.2.3 Force-Displacement relations for multi-TMP of α: 45° and 70°

Multi-TMP of α of 45° and 70° are considered here. The force-displacement curves for these two configurations with a constant set of values for the other parameters were generated.

The constant set of values are as follows: $l = 40$ mm; $m = 30$ mm; $d = 30$ mm; $N = 7$; $N_B = 4$; $N_W = 5$; The same four different initial configurations as the single TMP, defined by 4 different θ_M^0 were also considered. The force-displacement curves for the above configurations for the three directions of compression are shown in figure 5.6

The axial force-displacement curves of the multi-TMP are shown in parts A and B of figure 5.6. The behavior is similar to that of the single TMP for all configurations. It also shows the unique negative stiffness characteristic as the single TMP.

The lateral force-displacement curves are shown for $\alpha = 45°$ and $\alpha = 70°$ in parts C and D of figure 5.6 respectively. It is plotted for $\alpha = 45°$ and $70°$ for four different initial folding angles θ_M^0. The behavior of multi-TMP of $\alpha = 45°$ is similar to that of the single TMP of $\alpha = 45°$ for all configurations. The multi-TMP structure of $\alpha = 70°$ also shows tunable load capacity in the lateral direction as the single-TMP.

The plot showing the behavior of the multi-TMP structure for $\alpha = 70°$ and in either side of the critical point is shown in figure 5.7.

It was found that the critical point for the multi-TMP of the considered configuration is different from that of single TMP. The critical point for single TMP was $63°$ whereas for multi TMP it is $67°$. The reason for this shift has been found to be the differences in breadth of the single TMP and multi TMP. The main reason behind the tunable load capacity is the existence of a local maximum point in the Breadth vs θ_M curve. It can be seen from figure 5.8 that the maximum points of breadth are different for single and multi-TMP. This is because of the way in which the single TMP cells are stacked up on each other in the breadth direction.

Thus the multi-TMP structure also can be tuned for high or low load capacity under lateral compression.

The transverse force-displacement curves for the multi-TMP are shown in parts E and F of figure 5.6. The behavior is similar to that of the single TMP for all configurations and the multi-TMP structure also shows rigid, high load capacity in the transverse direction in a similar fashion- the load to compress the structure beyond a point increases drastically.

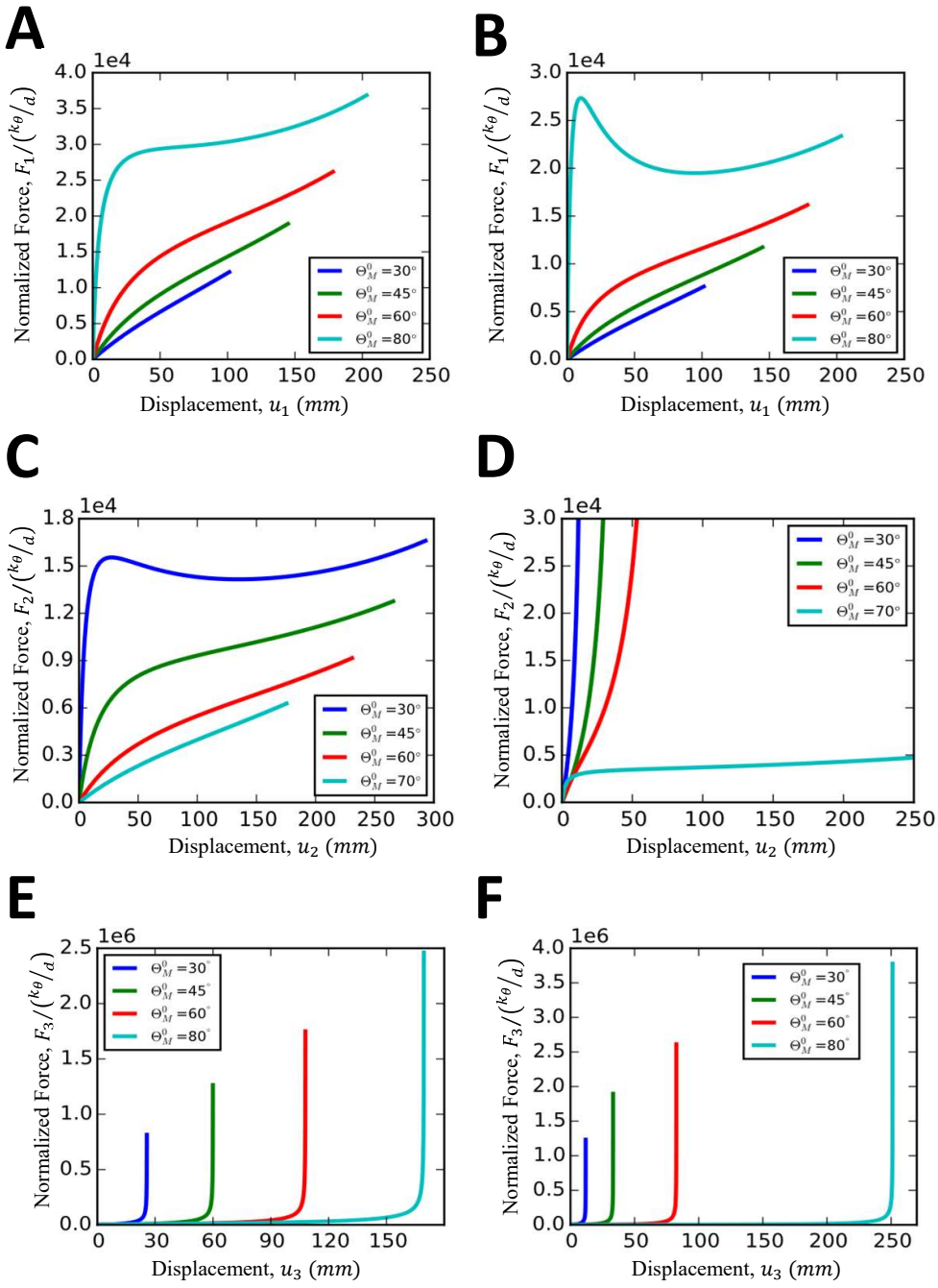

Figure 5.6: A) Axial Compression Force Displacement relation for multi-TMP of $\alpha = 45°$; B) Axial Compression Force Displacement relation for multi-TMP of $\alpha = 70°$; C) Lateral Compression Force Displacement relation for multi-TMP of $\alpha = 45°$; D) Lateral Compression Force Displacement relation for multi-TMP of $\alpha = 70°$; E) Transverse Compression Force Displacement relation for multi-TMP of $\alpha = 45°$; F) Transverse Compression Force Displacement relation for multi-TMP of $\alpha = 70°$

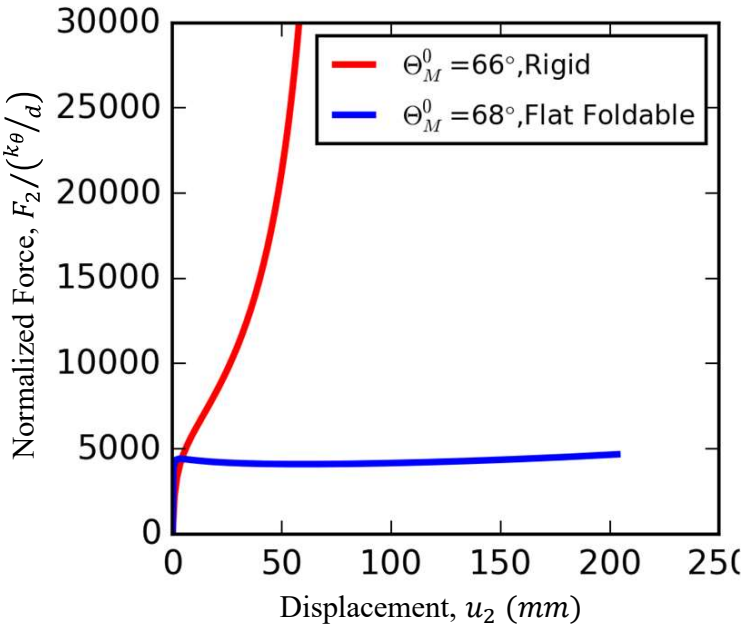

Figure 5.7: Flat Foldable and Highly Rigid configurations of multi TMP of $\alpha = 70°$ under Lateral Compression. $\theta_M^0 = 68°$ is flat foldable and $\theta_M^0 = 66°$ is highly rigid

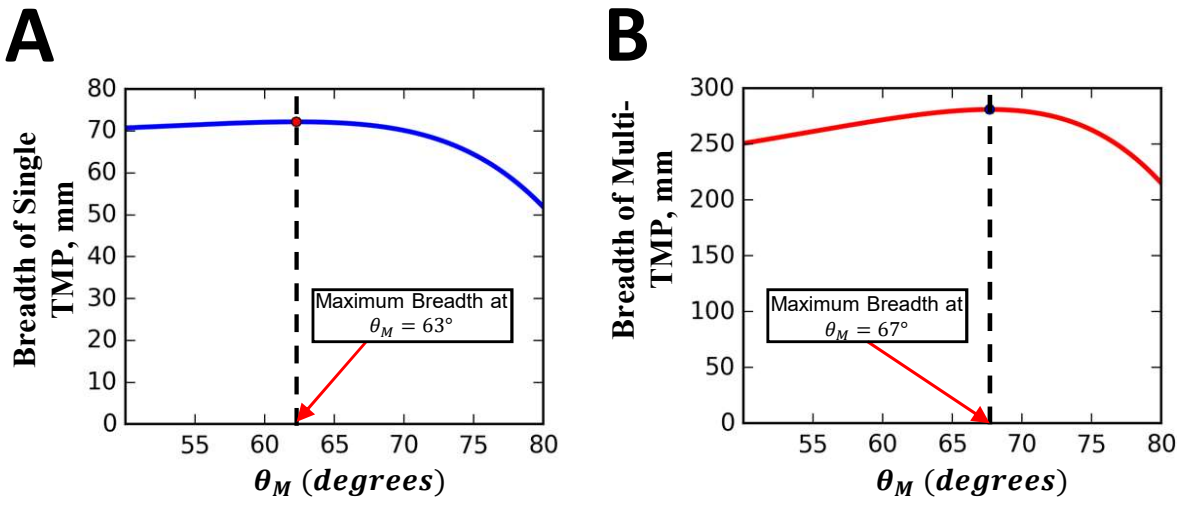

Figure 5.8: Breadth vs θ_M for A) Single TMP and B) multi TMP. The θ_M at which Maximum breadth is attained differs between the Single and multiTMP and hence the shift in critical folding angle

Thus the extension of single TMP force-displacement relations predict the same behavior for multi-TMP as well in terms of load capacity in the three directions. Now it is also clear that the structure exhibits drastically different levels of rigidity in the three directions similar to the single TMP. Thus the multi structure should also show anisotropic stiffness . To verify whether the multi-structure also exhibits anisotropic behavior and possibly tunable anisotropicity, the stiffness of the structure is computed analytically for whole range of initial configurations in the three directions and compared. This is explained in next section

5.3 Anisotropicity

Stiffness of the multi-TMP structure is computed as the derivative of force with respect to displacement and the formulae are as in eq.(3.13)

The stiffness is computed for the force-displacement relations of all three directions of loading and for the whole range of initial configurations, each of which is characterized by a distinct θ_M^0, in each loading direction for multi-TMP of configuration: $l = 40$ mm; $m = 30$ mm; $d = 30$ mm; $N = 7$; $N_B = 4$; $N_W = 5$.

Figure 5.9 shows the analytical stiffness of the three loading directions plotted for all initial configurations of the multi-TMP. The plot is similar to that of the single TMP except that the indeterminate point in lateral stiffness had shifted to $\theta_M^0 = 67^\circ$ which is the critical folding angle for multi-TMP. In this case of multi-TMP, the stiffness in the three directions are quite close to each other for initial configurations between $\theta_M^0 = 40^\circ \; and \; 50^\circ$ .Thus it can be concluded that the multi-TMP structure also exhibits tunable anisotropic behavior.

Thus to sum up, the multi-TMP structure shows similar relative load capacity in the three directions of loading as the single TMP. It also exhibits the tunable load capacity under lateral compression. The critical point will be different for multi-TMP when compared to single TMP because of variation in breadth caused by the stacking. The structure is also found to show anisotropic stiffness. These properties make the structure perfect for deployable yet load supporting structures. Some of the prospective applications for this structure are discussed in the final chapter.

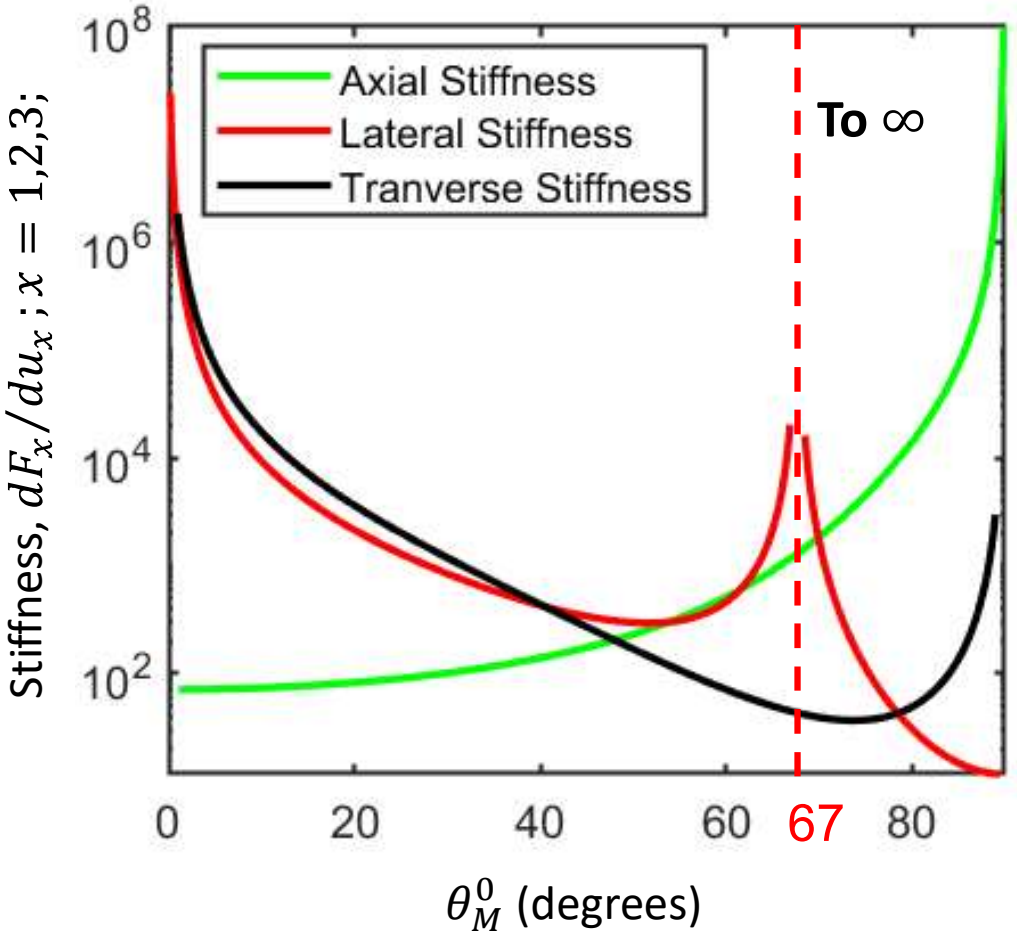

Figure 5.9: Analytical Stiffness of multi-TMP in three directions of loading, showing tunable Anisotropicity

Chapter 6

CONCLUSION

6.1 Application prospects

It has been understood that the TMP structure exhibits tunable load carrying capacity and anisotropic stiffness. These characteristics makes it an excellent choice for deployable yet load supporting structure. So this structure can be used for all those applications discussed in the introduction. There are some other application areas as well which were identified previously [14] and explained here. The tunable load carrying or rigidity behavior of the TMP structure makes it an option for designing emergency rafts which can be stored compactly in its flat folded state thereby facilitating cruises ships and aeroplanes to carry more of them and such rafts can be deployed in the wink of an eye thus saving more lives in an emergency. It can also be utilized to develop overload protection features for safe-fail design applications. The varying load carrying capability in three loading directions and anisotropic stiffness behavior of the structure can be utilized to design foldable furniture and portable structures. The TMP is also a good alternate option to design energy absorbers as it is foldable in one direction.

6.2 Summary of work

The novel behavior of an origami based structure called Tachi-Miura Polyhedron(TMP) is studied in the quest for a deployable yet load supporting structure. The response of the Tachi-Miura Polyhedron (TMP) to compression loading in three mutually perpendicular directions is modelled analytically using principle of virtual work. It is understood that the structure exhibits tunable load carrying capacity under lateral compression. The rigidity can be tuned by varying the initial main folding angle, θ_M^0. The analytical relations and the

tunability under lateral compression are verified by conducting compression load tests on paper prototypes. Then, the prospects of a multi-cell structure, in which multiple TMP single cells are combined together, are studied. The geometry of a particular type of multi-TMP structure is characterized and the force-displacement relations of the single TMP cells are extended to the multi-TMP structure. It is seen that the multi-TMP structure exhibits similar behavior as the single TMP cells under compression loading. In addition, the anisotropic nature of the structure is mathematically proven through the stiffness relations which are derived from the force-displacement relations. It is also understood that the structure will exhibit tunable anisotropic stiffness where the degree of anisotropicity can be controlled. The tunable load capacity ,anisotropic stiffness and bellows like folding makes the structure an ideal choice for deployable yet load supporting structure.

6.3 Future work

The multi-cell TMP structure opens up a variety of applications for which the TMP structure can be used. In moving towards this goal, the experimental verification of the force-displacement relations for the multi-TMP will be the next step. Another direction can be manufacturing of the TMP structure using engineering materials like metals and mass manufacturing techniques.If achieved,this will serve as a major boost for the multi-TMP to be used for real time applications. There are many different ways the single TMP cells can be combined to make the multi-TMP structure of which one way is studied in this work. The other ways must be explored and they may show novel behavior as well. Another direction that would serve as a major boost to the real-time use of the structure will be actuation of the structure in its folding motion. This will enable automatic deployment of structure and add great value to the structure. To conclude, the first steps in the study of a novel origami structure has been taken in this work. There is a lot more exciting work to be done on this structure to carry it towards usage in realtime applications.

BIBLIOGRAPHY

[1] G Greschik and MM Mikulas. Design study of a square solar sail architecture. *Journal of Spacecraft and Rockets*, 39(5):653–661, 2002.

[2] Qiaofeng Chen, Zhan Yao, Yangqing Hou, and Houfei Fang. Design and testing of a space deployable mechanism. In *4th AIAA Spacecraft Structures Conference*, page 0176, 2017.

[3] Fabien Royer and Sergio Pellegrino. Ultralight ladder-type coilable space structures. In *2018 AIAA Spacecraft Structures Conference*, page 1200, 2018.

[4] Christopher Yu, Keenan Crane, and Stelian Coros. Computational design of telescoping structures. *ACM Transactions on Graphics (TOG)*, 36(4):83, 2017.

[5] YunHo Kim, Chunghyeon Choi, Sarath Kumar Sathish Kumar, and Chun-Gon Kim. Hypervelocity impact on flexible curable composites and pure fabric layer bumpers for inflatable space structures. *Composite Structures*, 176:1061–1072, 2017.

[6] Zhong You and Kaori Kuribayashi. A novel origami stent. In *Proceedings of Summer Bioengineering Conference*, pages 0257–0258, 2003.

[7] Simon D Guest and Sergio Pellegrino. Inextensional wrapping of flat membranes. In *Proceedings of the First International Seminar on Structural Morphology*, volume 25, 1992.

[8] Shannon A Zirbel, Mary E Wilson, Spencer P Magleby, and Larry L Howell. An origami-inspired self-deployable array. In *ASME 2013 Conference on Smart Materials, Adaptive Structures and Intelligent Systems*, pages V001T01A026–V001T01A026. American Society of Mechanical Engineers, 2013.

[9] Kenneth C Cheung, Tomohiro Tachi, Sam Calisch, and Koryo Miura. Origami interleaved tube cellular materials. *Smart Materials and Structures*, 23(9):094012, 2014.

[10] Koryo Miura and Tomohiro Tachi. Synthesis of rigid-foldable cylindrical polyhedral. *Symmetry: Art and Science, International Society for the Interdisciplinary Study of Symmetry, Gmuend, Austria*, 2010.

[11] Tomohiro Tachi. One-dof cylindrical deployable structures with rigid quadrilateral panels. In *Symposium of the International Association for Shell and Spatial Structures (50th. 2009. Valencia). Evolution and Trends in Design, Analysis and Construction of Shell and Spatial Structures: Proceedings*. Editorial Universitat Politècnica de València, 2010.

[12] Koryo Miura. The science of miura-ori: A review. In *4th International Meeting of Origami Science, Mathematics, and Education, RJ Lang, ed., AK Peters, Natick, MA*, pages 87–100, 2009.

[13] H Yasuda and J Yang. Reentrant origami-based metamaterials with negative poissons ratio and bistability. *Physical review letters*, 114(18):185502, 2015.

[14] Balakumaran Gopalarethinam and Jinkyu Yang. Origami-based tunable structures with simultaneously foldable and stiff behavior. In *2018 AIAA Aerospace Sciences Meeting*, page 0081, 2018.

[15] Elisa Boatti, Nikolaos Vasios, and Katia Bertoldi. Origami metamaterials for tunable thermal expansion. *Advanced Materials*, 29(26), 2017.

[16] Lorna J Gibson and Michael F Ashby. *Cellular solids: structure and properties*. Cambridge university press, 1999.